Article

Cell Reports

Tumor-associated macrophage heterogeneity is driven by tissue territories in breast cancer

Graphical abstract

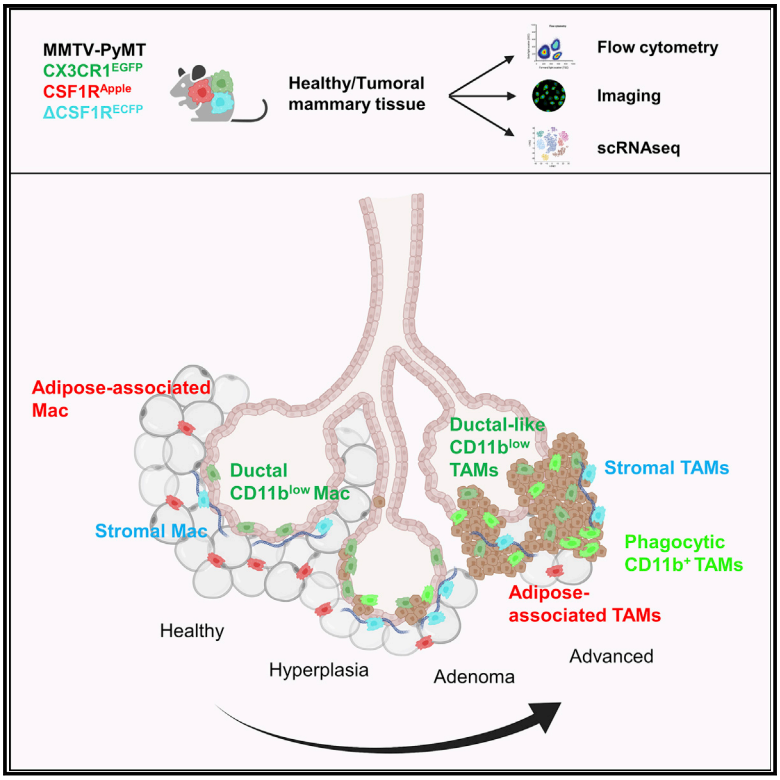

Authors

Marie Laviron, Maxime Petit, Eléonore Weber-Delacroix, ..., Christophe Combadière, Matthew F. Krummel, Alexandre Boissonnas

Correspondence

alexandre.boissonnas@upmc.fr

In brief

The origin of tumor-associated macrophage (TAM) heterogeneity is unclear. Laviron et al. show that TAM diversity is driven by the various tissue territories existing prior to tumor apparition and by the state of tumor malignancy. This provides a definition of TAM heterogeneity according to their spatial distribution *in situ*.

Highlights

- TAMs differentiate according to their localization *in situ*
- TAM heterogeneity is associated with resident TAM diversity prior to tumor development
- Orthotopic tumor models negate TAM diversity
- Similar heterogeneity is found in human breast TAMs

Laviron et al., 2022, Cell Reports *39*, 110865
May 24, 2022
https://doi.org/10.1016/j.celrep.2022.110865

CellPress

Cell Reports

CellPress
OPEN ACCESS

Article

Tumor-associated macrophage heterogeneity is driven by tissue territories in breast cancer

Marie Laviron,[1] Maxime Petit,[1] Eléonore Weber-Delacroix,[1] Alexis J. Combes,[2,3,4] Arjun Rao Arkal,[2,3] Sandrine Barthélémy,[1] Tristan Courau,[2,3] David A. Hume,[5] Christophe Combadière,[1] Matthew F. Krummel,[2] and Alexandre Boissonnas[1,6,*]

[1]Sorbonne Université, INSERM, CNRS, Centre d'Immunologie et des Maladies Infectieuses, Cimi-Paris, 75013 Paris, France
[2]Department of Pathology, ImmunoX Initiative, UCSF Immunoprofiler Initiative, University of California, San Francisco, San Francisco, CA 94143, USA
[3]UCSF CoLabs, University of California, San Francisco, San Francisco, CA 94143, USA
[4]Department of Medicine, University of California, San Francisco, San Francisco, CA 94143, USA
[5]Mater Research Institute-University of Queensland, Translational Research Institute, Brisbane, QLD 4101, Australia
[6]Lead contact
*Correspondence: alexandre.boissonnas@upmc.fr
https://doi.org/10.1016/j.celrep.2022.110865

SUMMARY

Tissue-resident macrophages adapt to local signals within tissues to acquire specific functions. Neoplasia transforms the tissue, raising the question as to how the environmental perturbations contribute to tumor-associated macrophage (TAM) identity and functions. Combining single-cell RNA sequencing (scRNA-seq) with spatial localization of distinct TAM subsets by imaging, we discover that TAM transcriptomic programs follow two main differentiation paths according to their localization in the stroma or in the neoplastic epithelium of the mammary duct. Furthermore, this diversity is exclusively detected in a spontaneous tumor model and tracks the different tissue territories as well as the type of tumor lesion. These TAM subsets harbor distinct capacity to activate CD8+ T cells and phagocyte tumor cells, supporting that specific tumor regions, rather than defined activation states, are the major drivers of TAM plasticity and heterogeneity. The distinctions created here provide a framework to design cancer treatment targeting specific TAM niches.

INTRODUCTION

Every adult tissue contains an abundant population of resident tissue macrophages distributed in a regular pattern with intimate interactions with other cells and extracellular matrix (Guilliams et al., 2020; Hume, 2006; Hume et al., 2019). Macrophages are also the most abundant immune cells of the tumor microenvironment (TME), which is composed of the stroma and the tumor parenchyma, and have been associated with bad prognosis in most cancers, including breast cancer (Condeelis and Pollard, 2006; Qian and Pollard, 2010). As a consequence, many proposed treatment modalities are directed toward suppression of tumor-associated macrophage (TAM) numbers or altering their function (reviewed in Cassetta and Pollard, 2018). Macrophage adaptation to the tumor environment has commonly been discussed in terms of a spectrum of polarization states from anti-tumor M1 to pro-tumor M2 (reviewed in Locati et al., 2020). However, the validity of the polarization model in cancer has been widely questioned (Hume and Freeman, 2014; Mujal et al., 2022; Xue et al., 2014). Therefore, a proper understanding of TAM intrinsic diversity related to their spatial localization over time is still warranted. During tumor growth, both tissue-resident macrophages and newly recruited monocyte-derived macrophages can give rise to TAMs, which instigated interrogations of their respective role in tumor progression (Franklin et al., 2014; Laviron and Boissonnas, 2019; Loyher et al., 2018; Müller et al., 2015; Zhu et al., 2017).

Within specific tissue territories, defined as the macrophage niche (Guilliams and Scott, 2017), mutual repulsion and competition for available growth factors may account for the distribution of macrophages (Guilliams et al., 2020; Hume et al., 2019). The link between tissue niche, ontogeny, and macrophage polarization has been well described for different organs at steady state (Bonnardel et al., 2019; Calderon et al., 2015). In the mammary gland, at least two populations of resident macrophages have been described: stromal and ductal macrophages (SMs and DMs, respectively), which are essential for the functions of the tissue (Dawson et al., 2020; Gouon-Evans et al., 2002; Jäppinen et al., 2019; Wang et al., 2020). Both were shown to derive from embryonic precursors, but SMs were slowly replaced by monocytes over life, while the majority of DMs were replaced in a spike at puberty and then established as long-lived cells (Dawson et al., 2020; Jäppinen et al., 2019).

Herein, we investigated the link between spatial distribution in different territories of breast cancer and the heterogeneity of TAMs. We associated single-cell RNA sequencing (scRNA-seq) to spatial mapping by imaging using a multiple transgenic fluorescent reporter mouse to discriminate mammary

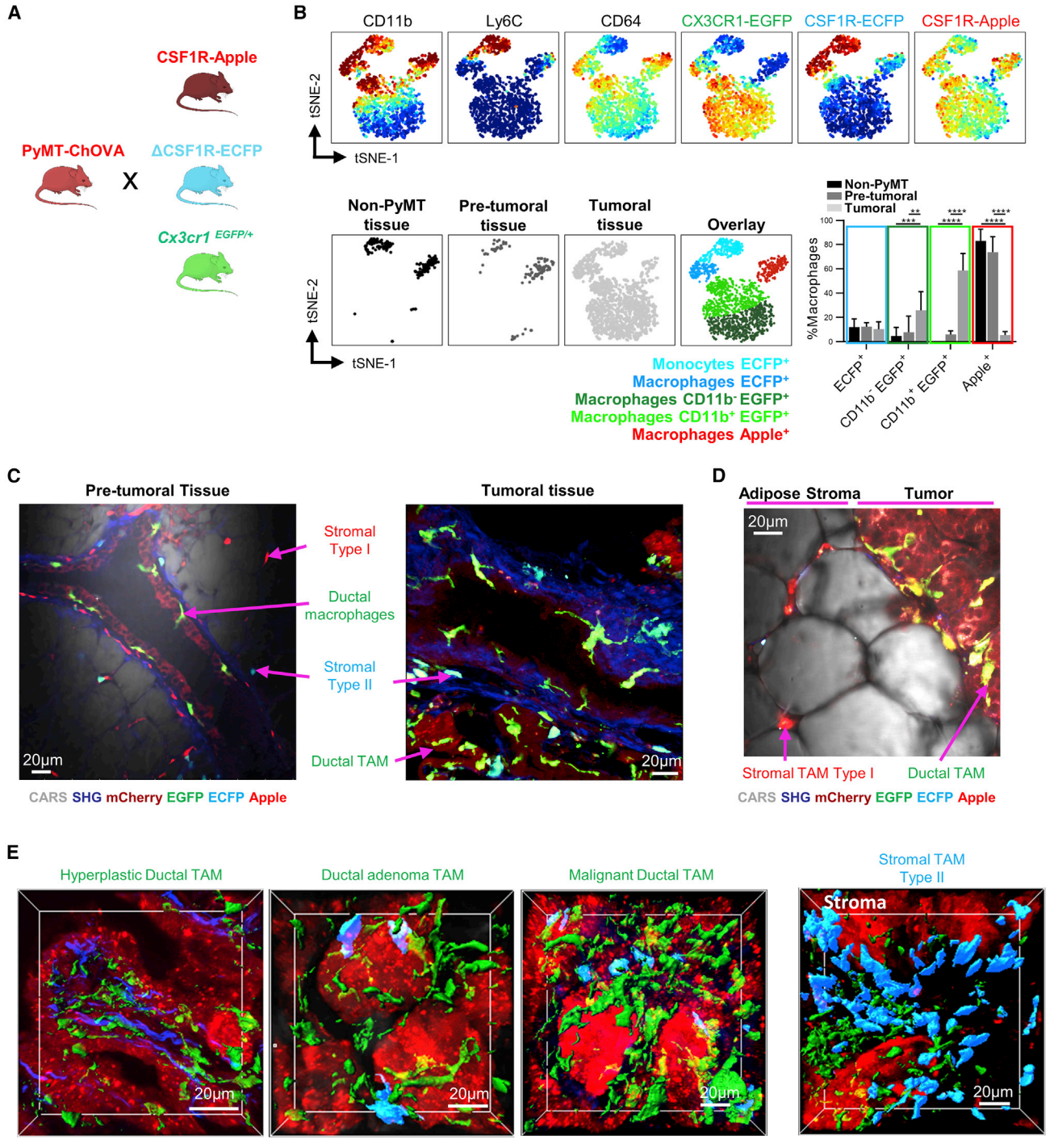

Figure 1. Breast macrophage niches evolve during tumor development

(A) MMTV-PyMT-mChOVA were crossed with *Cs1fr*-mApple, *ΔCsf1r*-ECFP, and *Cx3cr1*$^{kin/GFP}$ to generate a multi-fluorescent macrophage reporter mouse (PyMTFluo).

(B) Representative opt-SNE of flow cytometry analysis of the mammary monocyte/macrophage compartment shows the expression of the different markers and fluorescent reporters over tumor development. Non-PyMT represents non-tumoral mammary tissue from female fluorescent mice. Pre-tumoral tissue represents mammary tissue from <3-month-old tumor-free female PyMTFluo mouse. Tumoral tissue represents mammary tissue from >6-month-old tumor-bearing female PyMTFluo mice. The different macrophage subsets are color coded based on their relative expression of ECFP, EGFP, Apple, CD11b, and Ly6C. Histogram represents the percentages of each subset of fluorescent macrophages (n = 5–8 mice per group, mean ± SD are indicated). two-way ANOVA with Tukey's post test was performed. ** = $p < 0.01$, *** = $p < 0.001$, *** = $p < 0.0001$.

(legend continued on next page)

macrophage subsets in a spontaneous and a transplanted breast tumor model (Engelhardt et al., 2012; Guy et al., 1992). Our analysis reveals that ductal and stromal TAMs follow distinct differentiation pathways. Further functional diversity of these TAM subsets was detected according to different anatomical structures of the stroma and tumor malignancy. DMs associated with an advanced tumor stage were potent phagocytes but did not show efficient capacity to activate CD8 T cells compared with SMs. This spatial heterogeneity was lost in an orthotopic tumor model. Finally, similar subsets were identified in human breast tumor using a published scRNA-seq dataset (Pal et al., 2021). Altogether, those results provide insight into the spatial heterogeneity of TAMs and the role of the local microenvironment in defining their nature, which will help refine therapeutic strategies involving selective TAM targeting.

RESULTS

Breast macrophage niches evolve during tumor development

In mammary tissue, two different resident macrophage subsets were described in the literature associated with distinct locations: CD11b$^-$ DMs directly in contact with the epithelium of the mammary ducts and CD11b$^+$ SMs in the conjunctive and adipose mammary tissues (Bijnen and Bajénoff, 2021; Dawson et al., 2020; Jäppinen et al., 2019). We sought to determine the evolution of those niches in the MMTV-PyMT-mCherry model (named herein PyMT), which develops spontaneous multi-focal tumors from the mammary ductal epithelium at different stages recapitulating human breast tumor development (Attalla et al., 2021; Engelhardt et al., 2012; Lin et al., 2003). Up to 3 different fluorescent reporters dedicated to macrophage identification were added to the PyMT background: the MacApple transgene (Csf1r^{mApple} [Hawley et al., 2018]), the MacBlue binary transgene (ΔCsf1r-gal4/vp16/UAS-ECFP, referred to as ΔCsf1r^{ECFP} [Ovchinnikov et al., 2008]), and the knockin Cx3cr1$^{EGFP/+}$ [Jung et al., 2000]; Figure 1A). These three different reporters discriminate distinct macrophage subsets according to the relative expression of Apple, ECFP, and EGFP (Laviron et al., 2019). We used this fluorescent signature along with a panel of antibodies and performed t-distributed stochastic neighbor embedding (tSNE) reduction to monitor monocyte and macrophage accumulation in the mammary tissue from non-PyMT mice, 3-month-old PyMT with no detectable tumor at palpation, considered pre-tumoral tissue, and 6-month-old PyMT with palpable tumor nodules (Figure 1B). Healthy mammary tissue (non-PyMT and pre-tumoral) contained mainly CD11b$^+$Apple$^+$ macrophages and a small proportion of Ly6C^{hi} ECFP$^+$ EGFP^{low} monocytes and CD11b$^-$ EGFP$^+$ macrophages. The majority of CD11b$^+$Apple$^+$ macrophages were also MHC-II$^+$ (IA/IE), CD206$^+$, and CCR2$^+$ (Figure S1A). Two-photon imaging of fresh pre-tumoral mammary tissue confirmed that Apple$^+$ cells with typical macrophage morphology were located in the adipose and surrounding connective tissue defining a stromal population of macrophages associated with mammary fat (SM type I) (Figure 1C). Few round-shaped ECFP$^+$ cells were detected in the connective tissue, defining a second stromal population (SM type II). CD11b$^-$ MHC-II$^+$ EGFP$^+$ macrophages corresponded to DMs (Bijnen and Bajénoff, 2021; Dawson et al., 2020; Wang et al., 2020). Accordingly, these EGFP$^+$ cells were intra-epithelial (Figure 1C; Video S1). In tumoral tissue, CD11b$^-$ EGFP$^+$ macrophages massively accumulated along with the apparition of CD11b$^+$ EGFP$^+$ with lower expression of major histocompatibility complex (MHC) class II (Figures 1B and S1A). These cells did not remain only intra-epithelial but were mostly in close contact with tumor cells at all stages of tumor progression; hence, we still considered them ductal TAMs (Figures 1C, 1D, and S1B). Based on the description of the tumor stages by Lin and colleagues, hyperplastic lesions were characterized by increased mammary epithelium density with a detectable ductal lumen (Lin et al., 2003). The EGFP$^+$ ductal TAMs were elongated mostly intra-epithelial, parallel to the basement membrane of the mammary duct (Figures 1E and S1C). Adenoma lesions were characterized by tumor nodules with no more ductal lumen but a clear distinction of epithelial basement in which EGFP$^+$ ductal TAMs displayed stellate morphology at the periphery. Malignant lesions were characterized by a disrupted epithelial basement with invasive tumor organization where EGFP$^+$ ductal TAMs surrounded the tumor or were completely trapped within the tumor parenchyma (Figures 1E and S1C). Highly phagocytic EGFP$^+$ ductal TAMs were observed located in the lumen of the mammary duct similar to the ones observed during mammary epithelium involution post-weaning (Figure S1C) (Dawson et al., 2020). Upon tumor development, another macrophage subset defined as CD11b$^+$ ECFP$^+$ EGFP^{low} (for simplicity called ECFP$^+$) (Figure 1B) appeared and was mostly detected in stromal regions and was less in close contact with tumor cells (Figures 1C, 1E, S1B, and S1D). These ECFP$^+$ cells were composed of both monocytes and macrophages (Figures 1B and 1C). Numerous ECFP$^+$ cells were detected rolling and patrolling in the vasculature, as expected for monocytes (Video S2). They also accumulated nearby vascular regions within the tumor parenchyma and displayed a higher motility pattern compared with EGFP$^+$ cells (Video S3) but exhibited decreased velocity as they were moving closer to tumor cells (Video S4; Figure S1E). We assumed that ECFP$^+$ cells represent the most recently infiltrated monocytes and macrophages that progressively migrate and differentiate in the different regions of the tumor. Finally, upon tumor expansion, the Apple$^+$ SM type I were still mostly located to the adipose tissue at the periphery of the tumor or in smaller adipose islets (Figures 1C and S1B). To summarize, EGFP$^+$ cells were considered ductal TAMs further distinguished

(C) Two-photon laser scanning microscopy (TPLSM) images of the mammary tissue show the distribution of the different macrophage subsets in pre-tumoral and tumoral mammary tissue from PyMTFluo mice. Collagen was detected by second harmonic generation (SHG). Adipocytes were detected by coherent anti-stokes Raman spectroscopy (CARS) (Boissonnas et al., 2020). Scale bars, 20 μm.
(D) TPLSM image of mammary tumor border shows the restriction of stromal Apple$^+$ cells to adipose stroma. Scale bar, 20 μm.
(E) 3D TPLSM reconstructions show accumulation of EGFP$^+$ and ECFP$^+$ TAMs in the different types of tumor lesions: hyperplasia, adenoma, malignant ductal, and stroma. Scale bar, 20 μm. All panels all representative of at least n = 4 mice.
See also Figure S1.

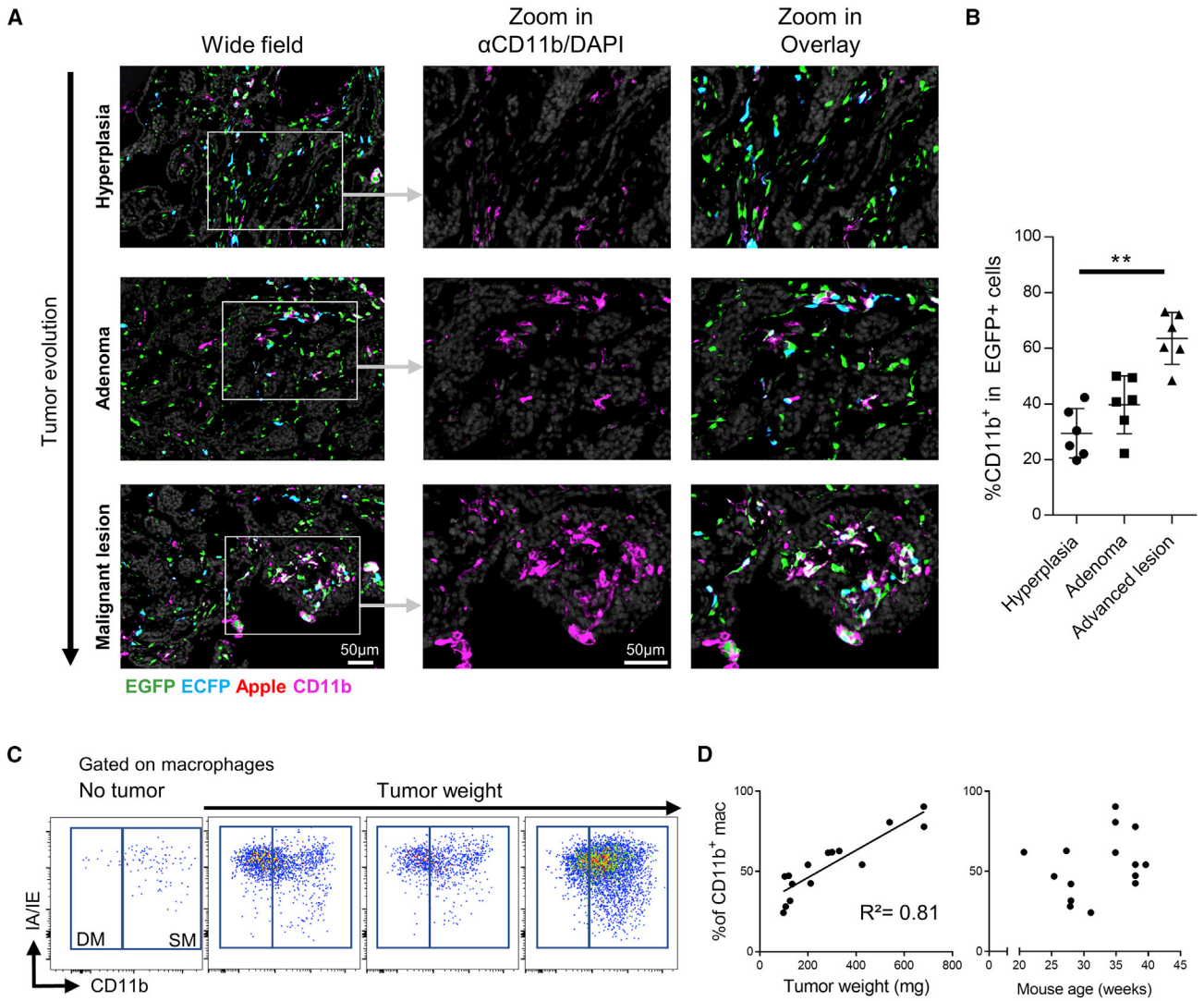

Figure 2. Ductal TAMs express CD11b$^+$ in malignant tumor lesions

(A) Representative wide-field images of hyperplastic, adenoma, and malignant tumor cryo-sections from PyMTFluo mice co-stained with anti-CD11b and DAPI (left column). Zoomed-in images (right columns) of each lesion type (white rectangles). Scale bar, 50 μm.

(B) Quantification of the percentage of CD11b$^+$ gated on EGFP$^+$ cells for each lesion (scatterplot represents mean ± SD, n = 6 tumors processed independently; each dot is a mean of 3–6 different lesions of the same tumor. Kruskal-Wallis with Dunn's multiple comparison test was performed). ** = $p < 0.01$.

(C) Representative dot plots show the relative proportion of CD11b$^-$ and CD11b$^+$ TAMs in PyMT tumor of different weights (from left to right dot plots: no tumor, <200 mg, between 200 and 400 mg, and >400 mg).

(D) Correlation of the proportion of CD11b$^+$ TAMs with tumor weight (left panel) or mouse age at time of study (n = 15 tumors from 10 mice; Pearson correlation coefficient is indicated).

by the emergence of CD11b$^+$ subset. Apple$^+$ cells represented an SM type I population associated with mammary fat. ECFP$^+$ cells represented both monocytes and a distinct tumor-induced SM type II population. In conclusion, we were able to identify, in mammary tumors, several subsets of TAMs exhibiting distinct localization related to the different macrophage niches existing prior to tumor development.

TAM composition shifts with tumor malignancy

EGFP$^+$ ductal TAMs comprised separable CD11b$^-$ and CD11b$^+$ subsets. To determine whether CD11b$^+$ are associated with a specific location or tumor progression, we quantified, by fluorescent imaging, CD11b expression, specifically on EGFP$^+$ cells associated with the three different stages of tumor evolution (Figures 2A and 2B). CD11b expression was significantly higher in EGFP$^+$ cells associated with malignant lesions compared with hyperplastic, consistent with the CD11b$^-$ phenotype of intra-epithelial macrophages in pre-tumoral tissue (Figure 2B). Moreover, this increase was confirmed using flow cytometry (Figure 2C). The relative proportion of CD11b$^+$ and CD11b$^-$ among the whole TAM compartment strikingly correlated with tumor weight but not with the age of the mouse (Figure 2D). These

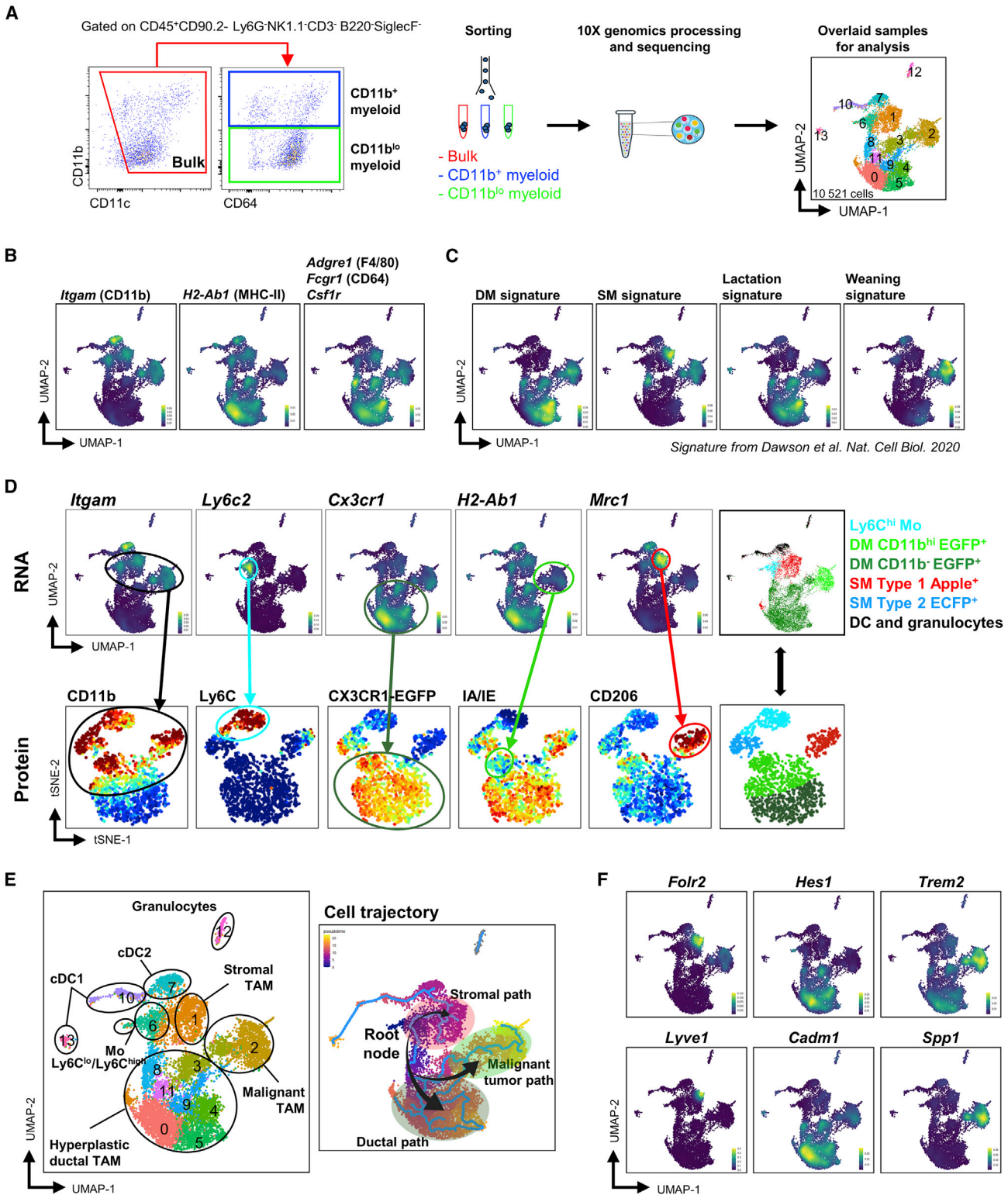

Figure 3. Stromal and ductal TAMs harbor localization-dependent transcriptomic profiles and differentiation paths

(A) 10X genomic processing and scRNA-seq of three sorted compartments (myeloid bulk or CD11b^{+}- or CD11b^{-}-enriched) from multiple-stage PyMT tumor pool (n = 4 female mice), and downstream processing following Seurat pipeline generated UMAP visualization after Louvain-graph-based clustering of the overlaid samples and identify 14 clusters.

(legend continued on next page)

results show that TAM composition shifts between hyperplastic and malignant tumor lesions.

Stromal and ductal TAMs follow distinct differentiation paths

To further characterize these different TAM subsets, three fractions of myeloid cells (total or CD11b$^+$ or CD11b$^-$ enriched) were sorted and subjected to scRNA-seq. We sorted the different subsets from a pool of tumors harvested from different PyMT mice, expecting to cover the different stages of tumor development (Figure 3A). The three fractions were normalized and combined, and a Louvain-graph-based clustering was performed that identified 14 clusters, represented using uniform manifold approximation and projection (UMAP) dimensional reduction method (Figure 3A). Differentially expressed genes were used to annotate each cluster (Figure S2A). First, consistent with protein expression, CD11b transcript (*Itgam)* was only observed in the CD11b$^+$-enriched compartment (Figures 3B, S2B, S2C, and S2D). The comparison of cell distribution showed that CD11b$^+$- and CD11b$^-$-enriched fractions clustered in different compartments and that the bulk overlapped both CD11b$^+$- and CD11b$^-$-enriched fractions (Figure S2B). Based upon a signature score from the combination of *Adgre1* (F4/80), *Fcgr1* (CD64), and *Csf1r* (CSF1R) expression, CD11b$^-$ and CD11b$^+$ compartments were both exhibiting macrophage signature (Figures 3B, S2B, and S2C). As expected (Figure S1A), *H2-Ab1* encoding a MHC class II gene was more highly expressed in CD11b$^-$ ductal TAMs (Figures 3B, S2C, and S2D). In order to support our findings based on microscopy, we first applied to our dataset the steady-state DM and SM signatures as well as lactation- and weaning-associated macrophage signatures defined by Dawson and colleagues (Dawson et al., 2020) (Figure 3C; Table S1). The DM signature mostly covered the CD11b$^-$ compartment including clusters 0, 4, 5, 8, 9, and 11 but also clusters 2 and 3 that belonged to a mix of CD11b$^+$ and CD11b$^-$ compartments. The lactation macrophage signature, which reflects an active proliferation state of DMs, covered the same clusters as the steady-state DMs. However, the weaning macrophage signature reflecting DMs participating in the involution of the mammary tissue through phagocytosis of milk-producing cells (Dawson et al., 2020) covered mostly cluster 2 and a fraction of cluster 3 (Figure 3C). The SM signature mainly covered cluster 1 (Figure 3C) but also a fraction of clusters 8 and 2, suggesting that these two clusters could be composed of both DMs and SMs or macrophages ongoing a transitory state between the stroma and the mammary duct. Dawson and colleagues also identified DC1 and DC2 signatures from sorted dendritic cells (DCs) of the mammary tissue (Table S1). These signatures applied to the PyMT dataset-associated cluster 7 to the DC2 signature and clusters 10 and 13 to the DC1 signature (Figures S2E and S2F). Finally, cluster 12 corresponded to a contamination of granulocytes.

Beyond the relationship established through the DM and SM signature overlaps, we next sought to match subsets identified by scRNA-seq, with the different TAM locations identified by imaging. We conclude that cluster 6 fits with ECFP$^+$Ly6C^{high} classical monocytes (cyan circle) based on the correlation *Itgam*$^+$/CD11b$^+$, *Ly6c2*$^+$/Ly6C$^+$, *Cx3cr1*^{low}/EGFP^{low} (Figure 3D) and supported by *Ccr2* expression (Figure S2F). Cluster 6 also included a small proportion of known non-classical monocyte markers *Nr4a1*$^+$, *Spn*$^+$, and *Treml4*$^+$ (Figure S2F). Clusters 0, 4, 5, 8, 9, and11 fitted with the EGFP$^+$ CD11b$^-$ hyperplastic ductal-associated macrophages (dark green circle) based on the correspondence of expression between transcript and protein *Itgam*^{low}/CD11b^{low}, *Cx3cr1*^{high}/EGFP^{high}, *H2-Ab1*^{high}/IA-IE^{high}. Clusters 2 and 3 were linked to EGFP$^+$ CD11b$^+$ malignant TAMs (light green circle) based on the correlation *Itgam*$^{+/-}$/CD11b^{int}, *H2-Ab1*^{low}/IA-IE^{low}, *Cx3cr1*^{high}/EGFP^{high}. Finally, cluster 1 was linked to the stromal type I TAMs (red circle) based on the correlation *Itgam*$^+$/CD11b$^+$, *Mrc1*$^+$/CD206, *H2-Ab1*^{high}/IA-IE^{high}, *Cx3cr1*$^-$/EGFP$^-$ (Figure 3D).

To address the relationship between the different macrophage subsets, we performed a pseudotime trajectory analysis to model the differentiation trajectories of each subset (Figure 3E). Franklin and colleagues used parabiosis experiment to confirm that peripheral monocytes contribute significantly to the accumulation of TAMs in the PyMT model (Franklin et al., 2014). Hence, we identified monocytes as the root node of the trajectory and defined two different paths evolving from this root. The stromal TAM path was linking monocytes to stromal TAMs and the ductal path was linking monocytes to ductal TAMs through cluster 8 (Figure 3E). Interestingly cluster 8 shared both stromal and ductal signatures, supporting this cluster as an intermediate state of stromal TAMs at the vicinity of the ductal epithelium.

While cluster 6 clearly identified monocytes, we were not able to clearly discriminate both subsets of stromal TAMs. To distinguish their transcriptomic profiles, we focused our analysis on clusters 1 and 6 corresponding to stromal TAMs and monocytes, respectively (Figures 3C and 3D) and performed a *de novo* clustering analysis to increase resolution. This sub-clustering generated 4 distinct clusters (Figure S3A). As done previously, we correlated the expression of *Ly6c2*, *Cx3cr1*, *H2-Ab1*, and *Mrc1* transcripts with their protein expression on the gated population. We recovered monocytes (*Ly6c2*$^+$/Ly6C$^+$, *H2-Ab1*^{low}/IA-IE^{low}) and Apple$^+$ SM type I (*Mrc1*$^+$/CD206$^+$), and we were able to assign the two other clusters to the ECFP$^+$ SM type II subset according to Cx3cr1$^+$/EGFP$^+$, *H2-Ab1*$^+$/IA-IE$^+$, and *Mrc1*$^+$/CD206$^+$,

(B) UMAP visualizations show specific gene expressions or gene signatures.
(C) UMAP visualization of the transcriptomic signatures of ductal macrophages (DMs), stromal macrophages (SMs), lactation, and weaning, obtained from Dawson et al. (2020).
(D) scRNA-seq-based UMAP (RNA) and flow-cytometry-based opt-SNE (protein) cross-analysis of selected transcripts and corresponding phenotypic markers. Color gates indicate corresponding subsets. Corresponding subsets are color coded accordingly.
(E) Trajectory analysis shows lineage relationships between the clusters. The monocyte cluster constitutes the root node of the trajectory.
(F) UMAP visualization of the relative expression of indicated transcript.
See also Figures S2 and S3.

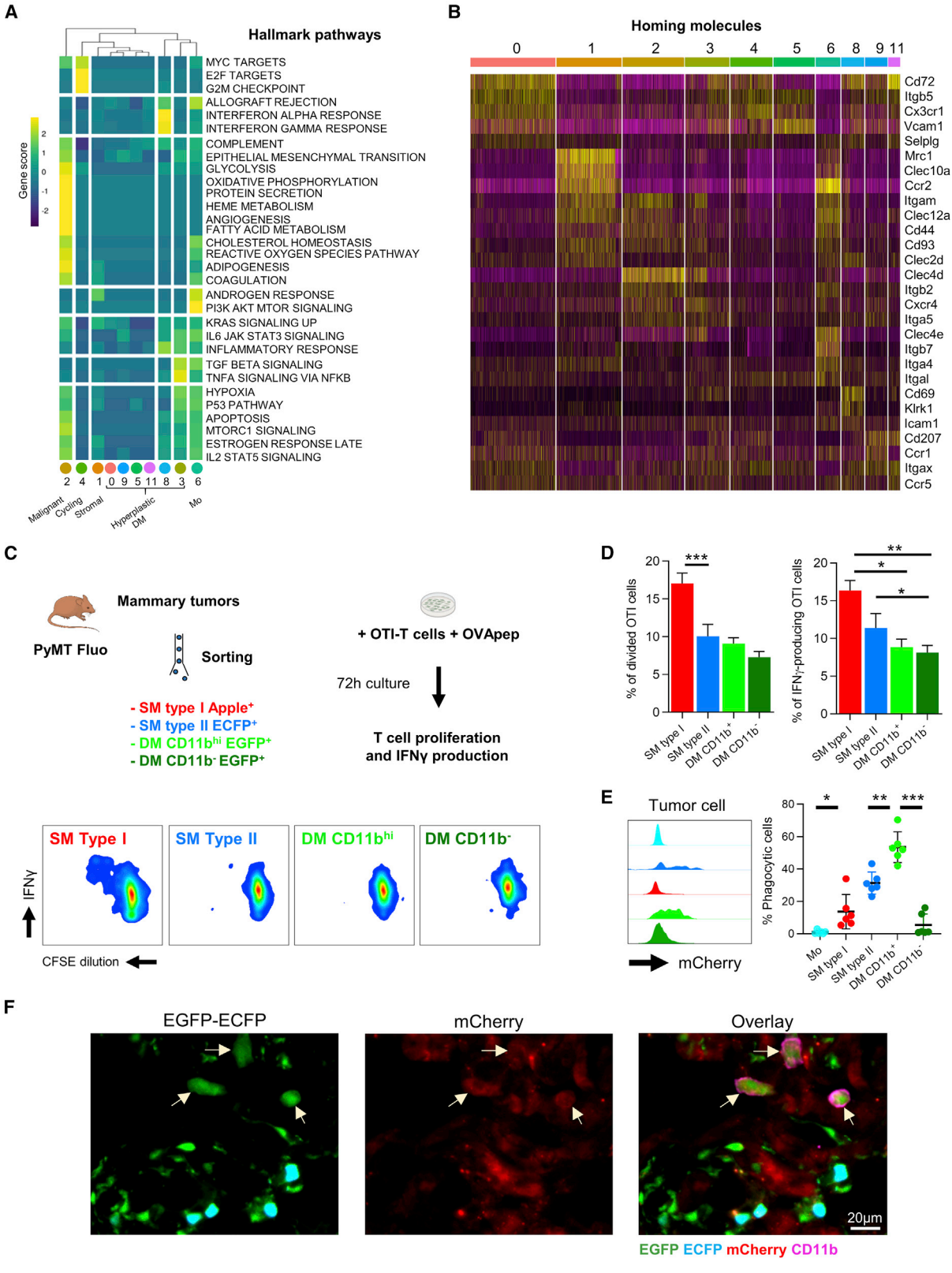

(legend on next page)

fitting with the phenotype observed by flow cytometry (Figures S3A–S3C). Pseudotime analysis on the sub-clustering of the stromal TAMs suggested a linear path from monocytes to stromal type I and II TAMs, suggesting that monocytes may differentiate into both types of stromal TAMs (Figure S3D). Following the ductal path, a circular relationship was shown in the region of hyperplastic ductal TAMs, suggesting a contribution of local proliferation. This was supported by cell-cycle analysis by flow cytometry using Topro3 to stain the DNA, showing that cycling CD11b^{-} TAMs represented the vast majority of cycling macrophages (Figures 3E and S3E). In contrast, local proliferation weakly contributed to the maintenance of SM type I macrophages, which might explain their relative loss along tumor evolution (Figure S3E). Finally, from the hyperplastic ductal TAM clusters, an alternative path throughout cluster 3 led to malignant tumor TAMs identified in cluster 2 (Figure 3E).

Previous studies have highlighted different markers discriminating TAM subsets in different tumor types in both human and mouse. We addressed whether these markers were also linked to different populations in our model. *Hes1*, *Folr2*, and *Lyve1* expression was attributed to an embryonic-like macrophage profile (Mulder et al., 2021; Sharma et al., 2020), while *Trem2*+ and *Spp1*+ macrophages were of monocytic origin and associated with pro-tumoral functions (Cheng et al., 2021; Katzenelenbogen et al., 2020; Mulder et al., 2021; Nalio Ramos et al., 2022). We found *Folr2* and *Lyve1* specifically in *Mrc1*+ SMs, and *Hes1* expression was found in hyperplastic ductal TAMs, along with *Cadm1*. *Trem2* and *Spp1* were observed in malignant TAMs (cluster 2), consistent with previous observations (Figures 3F and S3B).

In conclusion, TAMs accumulate through monocyte recruitment and local proliferation and progressively acquire specific transcriptomic signatures depending on their localization in distinct territories of the tumor stroma and the state of tumor malignancy.

TAM niches are associated to functional diversity

To further investigate whether the spatial heterogeneity of TAMs is associated with a specific functional profile of these different TAM subsets, we looked at the differential gene expression (DGE) between all clusters and performed a gene set enrichment analysis (GSEA) (Figure 4A). Hyperplastic DMs from cluster 4 exhibited a highly cycling score, confirming the local proliferation of CD11b^{-} TAMs. The intermediate cluster between monocytes and DMs (cluster 8) was associated with inflammatory response and strong interferon (IFN)-responsive scores (Figure 4A). SMs (cluster 1) were associated with relatively active adipogenesis, fatty-acid metabolism, and response to hormones, which is consistent with their location around the adipocytes. Hyperplastic DMs leading toward malignant DMs presented specific transforming growth factor β (TGF-β) and tumor necrosis factor α (TNF-α) signaling pathway scores and were also associated with the strongest hypoxic score. Finally, malignant DMs were associated with biological hallmarks mostly linked to active metabolism (glycolysis, oxidative phosphorylation, protein secretion, fat metabolism) but also tumor-associated environment (epithelial-to-mesenchymal transition [EMT], apoptosis, angiogenesis, hypoxia, reactive oxygen species) (Figure 4A). In order to better discriminate the functions among stromal TAMs, we used the DGE among the sub-clustering obtained in Figure S3A for a second GSEA (Figure S4A). Ly6C^{high} monocytes represented the most active subset with high score in IFN responses, glycolysis, and oxidative phosphorylation reflecting active energetic metabolism. ECFP^{+} SM type II showed a high angiogenesis signature, which might reflect their recent infiltration into the tumor.

TAM heterogeneity is commonly discussed in terms of an M1/M2 polarization spectrum. To test this model in our data, we selected a list of genes commonly related to macrophage polarization (Biswas and Mantovani, 2010; Cassetta et al., 2019; Cheng et al., 2021; Roberts et al., 2016) (Table S2). Correlation of expression between these genes across all individual cells was determined. Overall, correlation scores were low, and hierarchical clustering did not discriminate convincing M1- or M2-associated sets of genes, with the exception of two modules (correlation score >0.7) (Figure S4B). The first module defined by *Lyve1*, *Il10*, *Cd163*, and *Ccl24* identified a fraction of the *Mrc1*$^{+}$ cluster 1 corresponding to SMs (Figure S4C). The second module defined by *Arg1*, *Arg2*, and *Mmp9* highlighted a fraction of malignant TAMs (Figure S4C). Individual gene expression across the different clusters confirmed the absence of a clear-cut canonical M1 or M2 profile (Figure S4D), suggesting that the spatial localization of TAMs does not seem to reconcile the M1 or M2 nomenclature.

To refine the analysis and seek further markers of TAM heterogeneity, we selected a set of transcripts encoding cell surface molecules involved in homing, adhesion, and migration, obtained from the HUGO database (Table S3). Hierarchical clustering of the relative expression of their transcripts confirmed that TAM subsets display specific patterns changing with tissue localization and tumor progression (Figure 4B). We sought to identify the inherent transcription factor (TF) involved according to the transcriptomic profile of each cluster (Figure S4E). Putative role STAT1, STAT2, IRF7, and IRF9, associated with IFNγ

Figure 4. TAM subsets exhibit distinct polarization

(A) Heatmap of hierarchical clustering of the different biological hallmark k/K scores obtained from GSEA for monocyte and macrophage clusters (DC clusters were not included in the analysis).

(B) Heatmap of selected cell-surface-molecule-associated transcript expressions (lectins, integrins, and chemokine receptors) in TAM clusters.

(C) Layout of *in vitro* co-culture experiments of TAMs and OT-I T cells.

(D) Percentage of divided and IFNγ-producing T cells after 3 days of culture. Bar represent mean ± SEM pooled from three independent experiments. One-way ANOVA with multiple comparison test was performed.

(E) *In vivo* phagocytosis of mCherry^{+} tumor debris by TAM subsets (n = 6 mice processed independently, mean ± SEM are indicated, one-way ANOVA with multiple comparison test was performed).

(F) Immunofluorescence of CD11b expression by phagocytic TAMs. Scale bar, 20μm. *, **, *** = $p < 0.05$, <0.01, <0.001 respectively.

See also Figure S4.

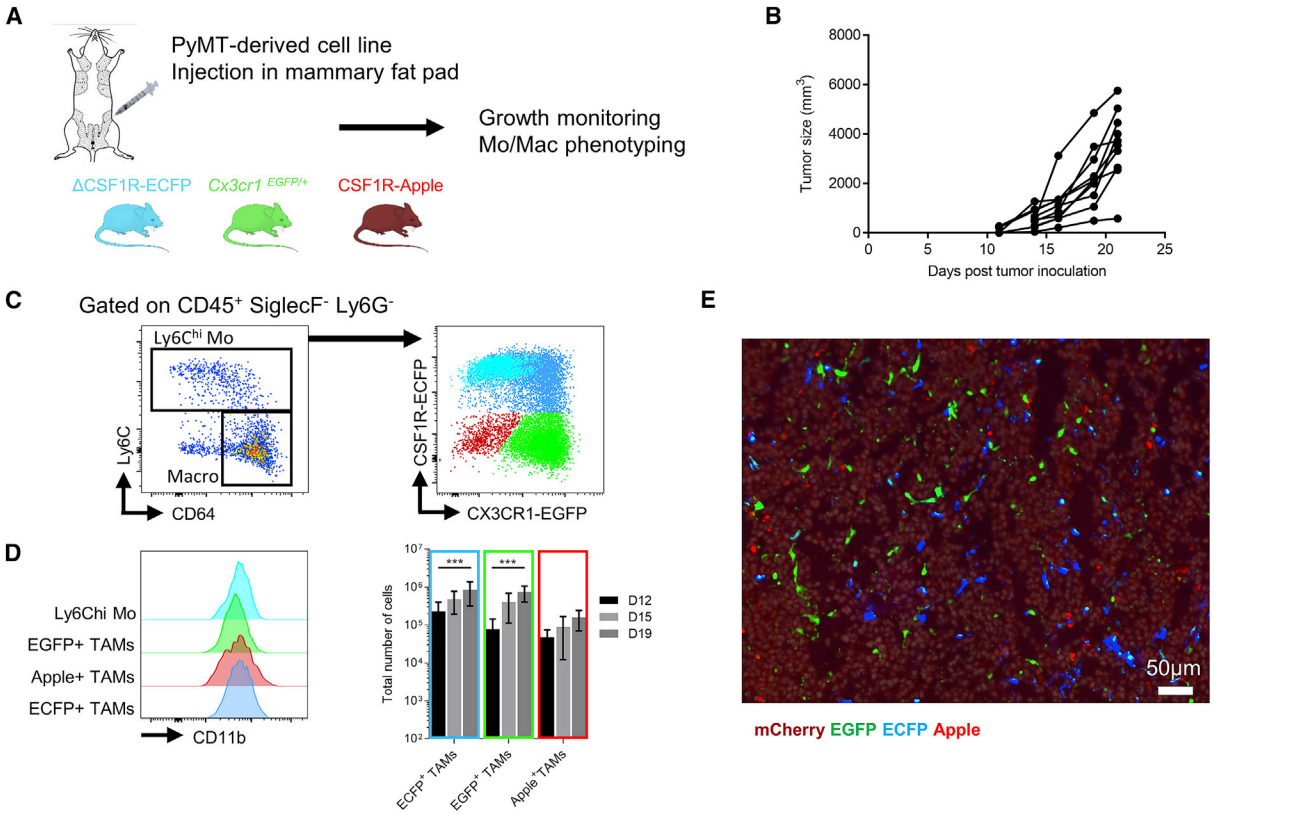

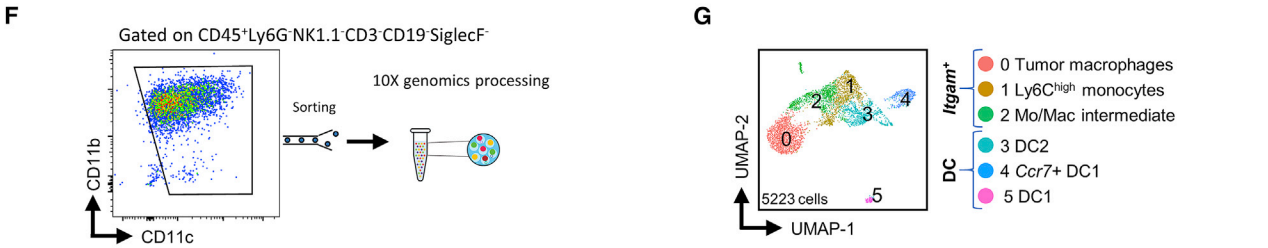

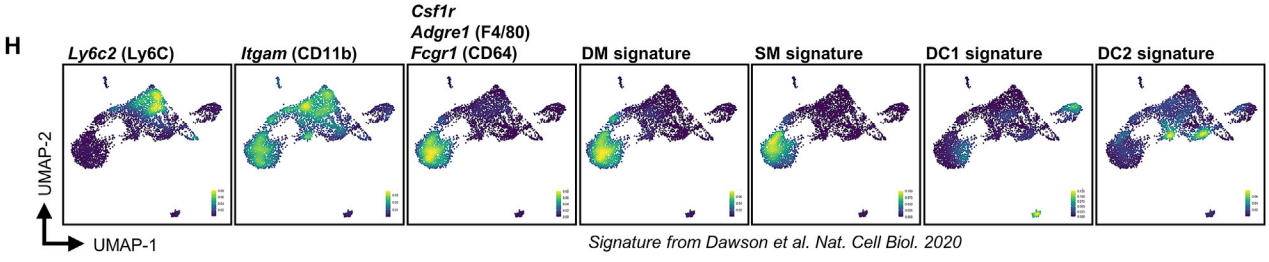

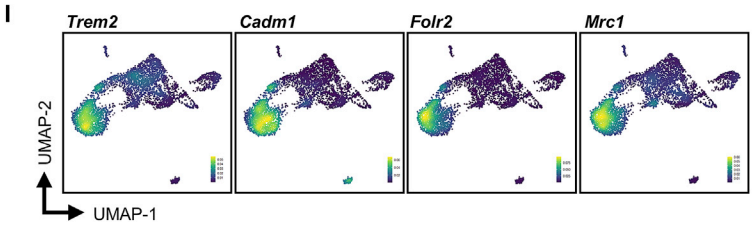

(legend on next page)

response (Kovarik et al., 1998), were associated with the intermediate monocyte/DM cluster (cluster 8). STAT3, associated with immune suppression (Hughes and Watson, 2018; Hughes et al., 2012) but also mammary gland involution (Sargeant et al., 2014), was found in the cluster of hyperplastic DMs leading to malignant DMs. The proliferation state of hyperplastic DM from cluster 4 was also confirmed by putative role of MYC and E2F4.

To gain further insights on their function beyond their different transcriptomic profile, we sorted each TAM subset from a pool of PyMT tumors, loaded them with exogenous ovalbumin (OVA) peptide SIINFEKL, and co-cultured them with OT-I T cells for 3 days (Figure 4C). We measured T cell proliferation and IFNγ production as a readout of their activation. In the presence of OVA peptide, SM type I were the most prone to induce T cell proliferation and IFNγ production by OT-I cells (Figure 4D). Co-culture of TAMs with sorted tumor cells did not show a significant impact on tumor cell proliferation or survival (data not shown). Taking advantage of mCherry expression by tumor cells, we next profiled the capacity of each TAM subset to participate in tumor cell clearance and thus exhibit mCherry fluorescence. Malignant CD11b^{+} DMs harbored the highest phagocytic potential among all subsets (Figure 4E). Imaging the phagocytic EGFP^{+} TAMs observed previously (Figure S1C), together with CD11b staining, strengthened this observation (Figure 4F). Despite this high phagocytic ability of the mCherry OVA tumor cells, no proliferation of OT-I was detected in the absence of exogenous OVA peptide for any TAM subsets (data not shown). This is consistent with previous observations showing that highly phagocytic macrophages are not potent antigen-presenting cells (Broz et al., 2014; Roberts et al., 2017). Overall, we conclude that the localization of TAM subsets drives their specific transcriptional programs and functional capacities in the TME.

TAM heterogeneity is reduced in an orthotopic model

We next addressed whether similar TAM heterogeneity can be recovered in an orthotopic tumor model. We performed orthotopic injection of breast tumor cells into the mammary fat pad as a model of the malignant stage of tumor development. PyMT cell line derived from a spontaneous MMTV-PyMT-mCherry tumor were injected into MacApple x MacBlue x Cx3cr1$^{EGFP/+}$ mice, and tumor growth and TAM composition were monitored (Figure 5A). Tumor nodules were palpable after 11 days and then grew exponentially to reach 4,000 mm^3 within a further 10 days (Figure 5B). Among monocytes, only the ECFP^{+}EGFP^{low} signature was recovered, whereas among macrophages, the three fluorescent signatures, also observed in the spontaneous tumors, were present (Figure 5C). No CD11b^{-}EGFP^{+} cells corresponding to DMs were recovered in this model, and ECFP^{+}TAMs and EGFP^{+}TAMs represent the most abundant subsets with a progressive accumulation with tumor growth (Figure 5D). The Apple^{+} TAMs remained the less abundant subset and did not significantly accumulate over tumor growth (Figure 5D). CD206 did not discriminate a specific subset of stromal TAMs, as observed in the spontaneous model, as the expression was similar in all subsets (Figure S5A). We analyzed the spatial distribution of these different TAM subsets by histological analysis. The structure of the tumor appeared as a dense aggregate of tumor cells with no distinction of stroma or hyperplastic mammary epithelium as observed in the spontaneous PyMT model (Figure 5E). The tumor was homogeneously infiltrated by the three fluorescent cell subsets.

We again performed scRNA-seq on sorted myeloid cells (Figure 5F). Louvain-graph-based clustering identified 5 clusters (Figure 5G). Clusters 3, 4, and 5 exhibited DC-associated signatures as defined by Dawson et al. (Figures 5G, 5H, and S5B) (Dawson et al., 2020). Cluster 1 corresponded to Ly6C^{hi} monocytes (*Itgam*$^{+}$, *Ly6c2*$^{+}$, *Ccr2*$^{+}$), while cluster 2 showed an intermediate monocyte/macrophage signature. Cluster 0 was the only cluster representing TAMs. DM and SM signatures both covered this cluster (Figure 5H), suggesting that only one main TAM differentiation path occurs in the orthotopic model in accordance with the observation that all TAMs develop in a rather homogeneous TME, mainly composed of tumor cells in this model. Additionally, the expression of *Trem2*, *Cadm1*, *Folr2*, and *Mrc1* was recovered in this TAM cluster, although their level of expression seemed to identify different cells within the cluster (Figure 5I). The GSEA based on the DGE of the 5 clusters revealed that cluster 0 was highly inflammatory and metabolically active, with a proliferative signature, resembling the cluster associated with malignant TAMs in the spontaneous model (cluster 2) (Figure S5C). Consistently, the projection of the signatures extracted from clusters 0, 1, and 2 of the orthotopic model to the UMAP of the spontaneous PyMT model confirmed the similarities with the cluster of malignant TAMs and hyperplastic TAMs (Figure S5D). We conclude that orthotopic models negate the impact of specific tissue location and drive TAMs toward a functional signature representative of advanced tumor malignancy.

Figure 5. TAM heterogeneity is associated with niche diversity

(A) The PyMT-derived cell line was injected orthotopically in the mammary fat pad of female Cs1fr-mApple x ΔCsf1r-ECFP x Cx3cr1$^{kin/EGFP}$ to mimic an orthotopic breast tumor model.

(B) Tumors were detectable from day 11 and grew in every mouse (n = 7).

(C) Dot plots show the fluorescent signatures among monocytes and macrophages in each subset of the orthotopic model.

(D) CD11b expression and absolute number of each subset in the whole tumor were quantified by flow cytometry at days 12, 15, and 19 post injection (mean ± SD are indicated, n = at least 3 mice per time point; representative of 3 independent experiments). Two-way ANOVA with Tukey's post test was performed. *** = $p < 0.001$.

(E) Representative cryo-sections of orthotopic mammary tumor shows tumor cell organization and fluorescent TAM distribution. Scale bar, 50 μm.

(F) Droplet-based scRNA-seq of sorted myeloid cells from the orthotopic PyMT tumors (n = 4 female mice), processed with the Seurat pipeline.

(G) UMAP visualization after Louvain-graph-based clustering shows 6 clusters.

(H) UMAP visualization of the expression of indicated transcripts, the macrophage signature (composed of *Adgre1*, *Fcgr1*, and *Csf1r* expression scores), and mammary-tissue-associated signatures of DM, SM, DC1, and DC2 from Dawson et al. (2020).

(I) UMAP visualization of the relative expression of indicated transcript.

See also Figure S5.

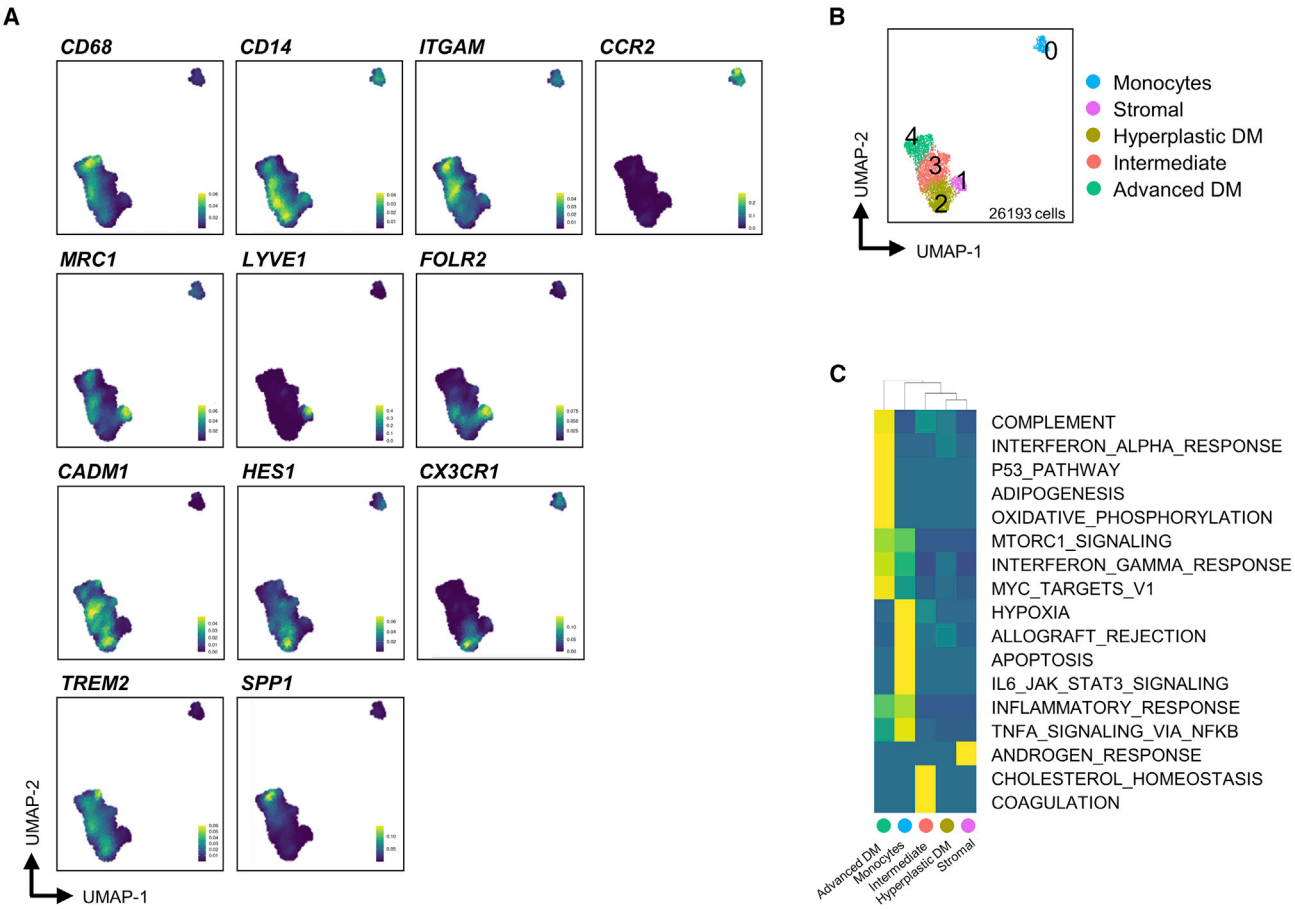

Figure 6. Human breast TAMs exhibit a niche-associated TAM diversity

(A) UMAP visualization of relative expression of indicated genes.

(B) UMAP visualization from Seurat pipeline after Louvain-graph-based clustering of the human dataset from Pal et al. (2021) (GEO: GSE161529).

(C) Heatmap shows hierarchical clustering of the different biological hallmark k/K scores obtained from GSEA.

Human breast TAMs exhibit similar diversity

As the MMTV-PyMT model has been described to recapitulate the different stages of development of human breast cancer, we sought to determine whether the TAM heterogeneity identified in this model could be reflected in human tumors. We used scRNAs-eq data from Visvader's group containing a diversity of cell types sequenced from different breast tumors (Pal et al., 2021). We focused our analysis on monocytes and macrophages by selecting them based on *CSF1R*, *CD68*, or *FCGR1A* expression and generated a UMAP representation of the concatenated tumor-associated myeloid cells. Louvain-graph-based clustering identified 10 clusters (Figure 6A). We applied the combination of markers that were used to identify distinct TAM subsets in PyMT mouse to the human dataset (Figure 6A). While those signatures were, in general, more heterogeneous, we retrieved a similar association. Monocytes were identified by expression of *ITGAM*, *CD14*, and *CCR2*. *FOLR2*$^{+}$ cells co-expressed *LYVE1* and *MRC1*, as observed in the stromal/adipose TAMs in the PyMT model (Figures 6A and 6B). A population of *ITGAM*^{low} *HES1*$^{+}$ *CADM1*$^{+}$ was recovered, suggesting that a profile similar to hyperplastic DMs in PyMT mice can be found in human breast tumors. Finally, advanced TAMs were identified by *TREM2*, *SPP1* expression. An intermediate population expressing markers from both hyperplastic- and advanced-like TAMs was identified (Figures 6A and 6B). Similar observations were recently made by Ramos and colleagues showing that *FOLR2* identify macrophages in the stroma in both healthy mammary tissue and malignant breast cancer, while *TREM2* and *SPP1* expression is specific to TAMs localized in the tumor nest (Nalio Ramos et al., 2022). SMs exhibited an androgen-response-associated transcriptomic signature, which is coherent with their association with the adipose stroma of the mammary tissue (Figure 6C). As in mice, an IFN-responsive cluster was also recovered in human tumors, corresponding to advanced-like TAMs. Altogether, these observations suggest that similar niche-associated patterns are found in human breast tumors.

DISCUSSION

Spontaneous tumors from the PyMT model generate multiple tumors from the mammary epithelium representative of the different stages of breast cancer in human tumors (Attalla

et al., 2021; Lin et al., 2003). Hence, this model provides both the spatial diversity of the mammary tissue and the temporal evolution of tumor transformation. Using three different reporter transgenes, we were able to distinguish multiple subsets of TAMs associated with distinct spatial and temporal territories. These different TAMs harbored conserved transcriptomic signatures of the two main macrophage populations isolated from the healthy mammary tissue, showing that environmental perturbation induced by tumor development does not fully reprogram TAMs from their original function and that TAM heterogeneity is spatially poised.

CD11b^{-} ductal TAMs, mainly detected in early tumors, were linked to monocytes through a differentiation path associated with IFN signaling signatures known to be involved in macrophage differentiation and in response to immune checkpoint blockade therapy (Benci et al., 2016; Delneste et al., 2003). This subset also exhibited a lactation macrophage signature, consistent with the idea that hyperplastic lesion resembles mammary tissue in active proliferation in which DMs and epithelial cells exert mutual benefits (Dawson et al., 2020; Van Nguyen and Pollard, 2002). Accordingly, the active proliferation of this subset suggests that they partially accumulate through local proliferation. We identified a secondary path leading to malignant ductal TAMs with high *Trem2* expression. Accordingly, TREM2 has been associated with bad prognosis and was suggested to regulate the immunosuppressive functions of TAMs of monocytic origin (Katzenelenbogen et al., 2020; Mulder et al., 2021). Although this subset reflects the presence of more advanced tumor lesions, these TAMs do not necessarily exert only pro-tumoral function. For instance, they harbored the most potent phagocytic capacity and a similar signature to DMs involved in tissue involution after weaning. TNF- and IFN-responsive clusters were identified in both human and mouse tumors, suggesting that these molecular axes are important paths in TAM activation and could represent promising therapeutic targets. Additionally, both pathways were recently shown to a define a specific tumor immune archetype (Combes et al., 2022).

A third independent path linking monocytes to stromal TAMs was identified. Stromal type I TAMs harbored potent T cell activation capacity *in vitro*, although they phagocyted less tumor cells than the CD11b^{+} ductal TAMs. This is likely to be associated with their respective tissue localization, with stromal type I TAMs restricted to the border of the tumor and in adipose islets while CD11b^{+} ductal TAMs are found in advanced tumor lesions. Similar observations were recently made in human breast cancer where FOLR2^{+} TAMs were positioned near blood vessels at the tumor periphery and co-localized with CD8 T cells (Nalio Ramos et al., 2022). We confirmed that the stromal type I TAMs exhibited higher capacity to activate OT-I T cells *in vitro* compared with other subsets only when adding exogenous cognate antigen. However, OT-I adoptive transfer *in vivo* has been shown to ineffective at rejecting the tumor (Engelhardt et al., 2012).

scRNA-seq has some limitations as a method to detect genuine heterogeneity in populations. Even the most highly expressed transcripts are detected in only a subset of cells (Summers et al., 2020), and clustering of cell types depends heavily on assumptions about the data structure. However, our clustering was mostly confirmed at the protein level by flow cytometry and recovered the main subsets observed by imaging. We showed that most TAM transcriptomic signatures poorly recovered the M1/M2 dichotomy, as shown recently in other mouse models (Mujal et al., 2022). CD206 is usually associated with M2-like phenotypes but is widely expressed by subsets of resident tissue macrophages including those of adipose tissue (Arendt et al., 2013; Silva et al., 2019; Summers et al., 2020; Wentworth et al., 2010). Although those TAMs were not in close contact with tumor nodules, adipose-associated macrophages are known to produce several inflammatory cytokines promoting tumor development (Arendt et al., 2013; Faria et al., 2020; Picon-Ruiz et al., 2017). In the orthotopic model, CD206 is expressed in a high frequency of TAMs regardless of their localization, but in human tumors, *Mrc1*$^{+}$ stromal TAMs were present in a proportion similar to the spontaneous model. This shows that orthotopic models tend to artificially bias TAM phenotypes. Indeed, TAM diversity was more restricted in the orthotopic model, which we argue is linked to the lack of niche variety and to a model representative of very progressive tumor. In the human dataset, we were able to recover a similar TAM diversity including the *HES1*$^{+}$, *FOLR2*$^{+}$, and *TREM2*$^{+}$ main subsets, with functional hallmarks comparable to the ones present in the mouse PyMT tumor. These subsets were recently identified in human breast tumors to reside in distinct niches (Nalio Ramos et al., 2022). Those observations emphasize the importance in considering TAMs in human tumors according to their tissue localization (Wu et al., 2021). The development of mass-cytometry imaging and spatial sequencing will further address this aspect.

Taken together, our data suggest that heterogeneity is not derived from any specific activation state but from the temporal profile adaptation of monocyte and macrophage to specific locations with the growing and developing tumor. Overall, our study proposes that TAM heterogeneity is directly related to the spatial diversity, which is shaped by the original structure of the tissue, the histological type of the tumor, and its developmental grade. Therefore, it will be key in the future to consider TAM spatial distribution to develop more tailored therapeutic strategies to precisely shape the tumor immune response.

Limitations of the study

Although we were able to link spatial heterogeneity of TAMs to their transcriptomic signature, the fluorescent profiles did not fully recover the granularity of TAMs reached by scRNA-seq but was, at least, associated to the main tissue territories. The reason why TAM subsets differentially expressed the fluorescent reporters as a result of their localization is still unclear. Further functional studies will help to determine how the surrounding signals regulate fluorescent reporter expression.

STAR★METHODS

Detailed methods are provided in the online version of this paper and include the following:

- KEY RESOURCES TABLE
- RESOURCE AVAILABILITY
  - Lead contact
  - Materials availability

SUPPLEMENTAL INFORMATION

Supplemental information can be found online at https://doi.org/10.1016/j.celrep.2022.110865.

ACKNOWLEDGMENTS

This work was supported by Association pour la Recherche contre le Cancer ARC "Projet labellisé" and by Cancéropole Ile-de-France "program Emergence 2020". INCa (2018-1-PLBIO-06-1) supported research activity and funding to M.P. M.L. was funded by Sorbonne University program "Idex SUPER" and Fondation pour la Recherche Médicale FRM. The authors thank UMS28 for the animal core facility and the two-photon microscopy and Doriane Foret and Thomas Van Hecke for animal breeding. Research in the D.A.H. laboratory was supported by the Mater Foundation. A.J.C., T.C., and M.F.K. were supported by UCSF Bakar ImmunoX and NIH (R01 U01).

AUTHOR CONTRIBUTIONS

Conceptualization M.L., A.J.C., C.C., M.F.K., and A.B.; methodology M.L., A.J.C, M.F.K., and A.B.; software M.L., M.P., A.J.C., A.A.R., and A.B.; formal analysis M.L., M.P., and A.B.; investigation M.L., M.P., E.W.-D., S.B., and T.C.; resources, A.A.R., D.A.H., and M.F.K.; data curation M.L., A.J.C., A.A.R., and A.B., writing – original draft, M.L. and A.B., writing – review & editing, M.L., M.P., A.J.C., D.A.H., M.F.K., and A.B.; supervision A.B. and M.F.K.; funding acquisition, A.B. and M.F.K.

DECLARATION OF INTERESTS

The authors declare no competing interests.

Received: September 10, 2021
Revised: April 4, 2022
Accepted: May 3, 2022
Published: May 24, 2022

REFERENCES

Alquicira-Hernandez, J., and Powell, J.E. (2021). Nebulosa recovers single cell gene expression signals by kernel density estimation. Bioinforma. Oxf. Engl., Btab003. https://doi.org/10.1093/bioinformatics/btab003.

Arendt, L.M., McCready, J., Keller, P.J., Baker, D.D., Naber, S.P., Seewaldt, V., and Kuperwasser, C. (2013). Obesity promotes breast cancer by CCL2-mediated macrophage recruitment and angiogenesis. Cancer Res. *73*, 6080–6093. https://doi.org/10.1158/0008-5472.CAN-13-0926.

Attalla, S., Taifour, T., Bui, T., and Muller, W. (2021). Insights from transgenic mouse models of PyMT-induced breast cancer: recapitulating human breast cancer progression in vivo. Oncogene *40*, 475–491. https://doi.org/10.1038/s41388-020-01560-0.

Benci, J.L., Xu, B., Qiu, Y., Wu, T.J., Dada, H., Twyman-Saint Victor, C., Cucolo, L., Lee, D.S.M., Pauken, K.E., Huang, A.C., et al. (2016). Tumor interferon signaling regulates a multigenic resistance program to immune checkpoint blockade. Cell *167*, 1540–1554.e12. https://doi.org/10.1016/j.cell.2016.11.022.

Bijnen, M., and Bajénoff, M. (2021). Gland macrophages: reciprocal control and function within their niche. Trends Immunol. *42*, 120–136. https://doi.org/10.1016/j.it.2020.12.006.

Biswas, S.K., and Mantovani, A. (2010). Macrophage plasticity and interaction with lymphocyte subsets: cancer as a paradigm. Nat. Immunol. *11*, 889–896. https://doi.org/10.1038/ni.1937.

Boissonnas, A., Louboutin, F., Laviron, M., Loyher, P.-L., Reboussin, E., Barthelemy, S., Réaux-Le Goazigo, A., Lobsiger, C.S., Combadière, B., Mélik Parsadaniantz, S., et al. (2020). Imaging resident and recruited macrophage contribution to Wallerian degeneration. J. Exp. Med. *217*, e20200471. https://doi.org/10.1084/jem.20200471.

Bonnardel, J., T'Jonck, W., Gaublomme, D., Browaeys, R., Scott, C.L., Martens, L., Vanneste, B., De Prijck, S., Nedospasov, S.A., Kremer, A., et al. (2019). Stellate cells, hepatocytes, and endothelial cells imprint the kupffer cell identity on monocytes colonizing the liver macrophage niche. Immunity *51*, 638–654.e9. https://doi.org/10.1016/j.immuni.2019.08.017.

Broz, M., Binnewies, M., Boldajipour, B., Nelson, A., Pollock, J., Erle, D., Barczak, A., Rosenblum, M., Daud, A., Barber, D., et al. (2014). Dissecting the tumor myeloid compartment reveals rare activating antigen presenting cells, critical for T cell immunity. Cancer Cell *26*, 638–652. https://doi.org/10.1016/j.ccell.2014.09.007.

Calderon, B., Carrero, J.A., Ferris, S.T., Sojka, D.K., Moore, L., Epelman, S., Murphy, K.M., Yokoyama, W.M., Randolph, G.J., and Unanue, E.R. (2015). The pancreas anatomy conditions the origin and properties of resident macrophages. J. Exp. Med. *212*, 1497–1512. https://doi.org/10.1084/jem.20150496.

Cao, J., Spielmann, M., Qiu, X., Huang, X., Ibrahim, D.M., Hill, A.J., Zhang, F., Mundlos, S., Christiansen, L., Steemers, F.J., et al. (2019). The single-cell transcriptional landscape of mammalian organogenesis. Nature *566*, 496–502. https://doi.org/10.1038/s41586-019-0969-x.

Cassetta, L., and Pollard, J.W. (2018). Targeting macrophages: therapeutic approaches in cancer. Nat. Rev. Drug Discov. https://doi.org/10.1038/nrd.2018.169.

Cassetta, L., Fragkogianni, S., Sims, A.H., Swierczak, A., Forrester, L.M., Zhang, H., Soong, D.Y.H., Cotechini, T., Anur, P., Lin, E.Y., et al. (2019). Human tumor-associated macrophage and monocyte transcriptional landscapes reveal cancer-specific reprogramming, biomarkers, and therapeutic targets. Cancer Cell *35*, 588–602.e10. https://doi.org/10.1016/j.ccell.2019.02.009.

Cheng, S., Li, Z., Gao, R., Xing, B., Gao, Y., Yang, Y., Qin, S., Zhang, L., Ouyang, H., Du, P., et al. (2021). A pan-cancer single-cell transcriptional atlas of tumor infiltrating myeloid cells. Cell *184*, 792–809.e23. https://doi.org/10.1016/j.cell.2021.01.010.

Combes, A.J., Samad, B., Tsui, J., Chew, N.W., Yan, P., Reeder, G.C., Kushnoor, D., Shen, A., Davidson, B., Barczak, A.J., et al. (2022). Discovering dominant tumor immune archetypes in a pan-cancer census. Cell *185*, 184–203.e19. https://doi.org/10.1016/j.cell.2021.12.004.

Condeelis, J., and Pollard, J.W. (2006). Macrophages: obligate partners for tumor cell migration, invasion, and metastasis. Cell *124*, 263–266. https://doi.org/10.1016/j.cell.2006.01.007.

Dawson, C.A., Pal, B., Vaillant, F., Gandolfo, L.C., Liu, Z., Bleriot, C., Ginhoux, F., Smyth, G.K., Lindeman, G.J., Mueller, S.N., et al. (2020). Tissue-resident

ductal macrophages survey the mammary epithelium and facilitate tissue remodelling. Nat. Cell Biol. https://doi.org/10.1038/s41556-020-0505-0.

Delneste, Y., Charbonnier, P., Herbault, N., Magistrelli, G., Caron, G., Bonnefoy, J.-Y., and Jeannin, P. (2003). Interferon-gamma switches monocyte differentiation from dendritic cells to macrophages. Blood *101*, 143–150. https://doi.org/10.1182/blood-2002-04-1164.

Dobin, A., Davis, C.A., Schlesinger, F., Drenkow, J., Zaleski, C., Jha, S., Batut, P., Chaisson, M., and Gingeras, T.R. (2013). STAR: ultrafast universal RNA-seq aligner. Bioinforma. Oxf. Engl. *29*, 15–21. https://doi.org/10.1093/bioinformatics/bts635.

Engelhardt, J.J., Boldajipour, B., Beemiller, P., Pandurangi, P., Sorensen, C., Werb, Z., Egeblad, M., and Krummel, M.F. (2012). Marginating dendritic cells of the tumor microenvironment cross-present tumor antigens and stably engage tumor-specific T cells. Cancer Cell *21*, 402–417. https://doi.org/10.1016/j.ccr.2012.01.008.

Faria, S.S., Corrêa, L.H., Heyn, G.S., de Sant'Ana, L.P., Almeida, R.D.N., and Magalhães, K.G. (2020). Obesity and breast cancer: the role of crown-like structures in breast adipose tissue in tumor progression, prognosis, and therapy. J. Breast Cancer *23*, 233–245. https://doi.org/10.4048/jbc.2020.23.e35.

Franklin, R.A., Liao, W., Sarkar, A., Kim, M.V., Bivona, M.R., Liu, K., Pamer, E.G., and Li, M.O. (2014). The cellular and molecular origin of tumor-associated macrophages. Science *344*, 921–925. https://doi.org/10.1126/science.1252510.

Gouon-Evans, V., Lin, E.Y., and Pollard, J.W. (2002). Requirement of macrophages and eosinophils and their cytokines/chemokines for mammary gland development. Breast Cancer Res. BCR *4*, 155–164. https://doi.org/10.1186/bcr441.

Guilliams, M., and Scott, C.L. (2017). Does niche competition determine the origin of tissue-resident macrophages? Nat. Rev. Immunol. *17*, 451–460. https://doi.org/10.1038/nri.2017.42.

Guilliams, M., Thierry, G.R., Bonnardel, J., and Bajenoff, M. (2020). Establishment and maintenance of the macrophage niche. Immunity *52*, 434–451. https://doi.org/10.1016/j.immuni.2020.02.015.

Guy, C.T., Cardiff, R.D., and Muller, W.J. (1992). Induction of mammary tumors by expression of polyomavirus middle T oncogene: a transgenic mouse model for metastatic disease. Mol. Cell. Biol. *12*, 954–961. https://doi.org/10.1128/mcb.12.3.954-961.1992.

Hawley, C.A., Rojo, R., Raper, A., Sauter, K.A., Lisowski, Z.M., Grabert, K., Bain, C.C., Davis, G.M., Louwe, P.A., Ostrowski, M.C., et al. (2018). Csf1r-mApple transgene expression and ligand binding in vivo reveal dynamics of CSF1R expression within the mononuclear phagocyte system. J. Immunol. Baltim. Md 1950. https://doi.org/10.4049/jimmunol.1701488.

Hughes, K., and Watson, C.J. (2018). The multifaceted role of STAT3 in mammary gland involution and breast cancer. Int. J. Mol. Sci. *19*, E1695. https://doi.org/10.3390/ijms19061695.

Hughes, K., Wickenden, J.A., Allen, J.E., and Watson, C.J. (2012). Conditional deletion of Stat3 in mammary epithelium impairs the acute phase response and modulates immune cell numbers during post-lactational regression. J. Pathol. *227*, 106–117. https://doi.org/10.1002/path.3961.

Hume, D.A. (2006). The mononuclear phagocyte system. Curr. Opin. Immunol. *18*, 49–53. https://doi.org/10.1016/j.coi.2005.11.008.

Hume, D.A., and Freeman, T.C. (2014). Transcriptomic analysis of mononuclear phagocyte differentiation and activation. Immunol. Rev. *262*, 74–84. https://doi.org/10.1111/imr.12211.

Hume, D.A., Irvine, K.M., and Pridans, C. (2019). The mononuclear phagocyte system: the relationship between monocytes and macrophages. Trends Immunol. *40*, 98–112. https://doi.org/10.1016/j.it.2018.11.007.

Jäppinen, N., Félix, I., Lokka, E., Tyystjärvi, S., Pynttäri, A., Lahtela, T., Gerke, H., Elima, K., Rantakari, P., and Salmi, M. (2019). Fetal-derived macrophages dominate in adult mammary glands. Nat. Commun. *10*. https://doi.org/10.1038/s41467-018-08065-1.

Jung, S., Aliberti, J., Graemmel, P., Sunshine, M.J., Kreutzberg, G.W., Sher, A., and Littman, D.R. (2000). Analysis of fractalkine receptor CX3CR1 function by targeted deletion and green fluorescent protein reporter gene insertion. Mol. Cell. Biol. *20*, 4106–4114.

Katzenelenbogen, Y., Sheban, F., Yalin, A., Yofe, I., Svetlichnyy, D., Jaitin, D.A., Bornstein, C., Moshe, A., Keren-Shaul, H., Cohen, M., et al. (2020). Coupled scRNA-seq and intracellular protein activity reveal an immunosuppressive role of TREM2 in cancer. Cell *182*, 872–885.e19. https://doi.org/10.1016/j.cell.2020.06.032.

Kovarik, P., Stoiber, D., Novy, M., and Decker, T. (1998). Stat1 combines signals derived from IFN-gamma and LPS receptors during macrophage activation. EMBO J. *17*, 3660–3668. https://doi.org/10.1093/emboj/17.13.3660.

Kowalczyk, M.S., Tirosh, I., Heckl, D., Rao, T.N., Dixit, A., Haas, B.J., Schneider, R.K., Wagers, A.J., Ebert, B.L., and Regev, A. (2015). Single-cell RNA-seq reveals changes in cell cycle and differentiation programs upon aging of hematopoietic stem cells. Genome Res. *25*, 1860–1872. https://doi.org/10.1101/gr.192237.115.

Laviron, M., and Boissonnas, A. (2019). Ontogeny of tumor-associated macrophages. Front. Immunol. *10*, 1799. https://doi.org/10.3389/fimmu.2019.01799.

Laviron, M., Combadière, C., and Boissonnas, A. (2019). Tracking monocytes and macrophages in tumors with live imaging. Front. Immunol. *10*, 1201. https://doi.org/10.3389/fimmu.2019.01201.

Lin, E.Y., Jones, J.G., Li, P., Zhu, L., Whitney, K.D., Muller, W.J., and Pollard, J.W. (2003). Progression to malignancy in the polyoma middle T oncoprotein mouse breast cancer model provides a reliable model for human diseases. Am. J. Pathol. *163*, 2113–2126. https://doi.org/10.1016/S0002-9440(10)63568-7.

Locati, M., Curtale, G., and Mantovani, A. (2020). Diversity, mechanisms, and significance of macrophage plasticity. Annu. Rev. Pathol. *15*, 123–147. https://doi.org/10.1146/annurev-pathmechdis-012418-012718.

Loyher, P.-L., Hamon, P., Laviron, M., Meghraoui-Kheddar, A., Goncalves, E., Deng, Z., Torstensson, S., Bercovici, N., Baudesson de Chanville, C., Combadière, B., et al. (2018). Macrophages of distinct origins contribute to tumor development in the lung. J. Exp. Med. *215*, 2536–2553. https://doi.org/10.1084/jem.20180534.

Macosko, E.Z., Basu, A., Satija, R., Nemesh, J., Shekhar, K., Goldman, M., Tirosh, I., Bialas, A.R., Kamitaki, N., Martersteck, E.M., et al. (2015). Highly parallel genome-wide expression profiling of individual cells using nanoliter droplets. Cell *161*, 1202–1214. https://doi.org/10.1016/j.cell.2015.05.002.

Mujal, A.M., Combes, A.J., Rao, A.A., Binnewies, M., Samad, B., Tsui, J., Boissonnas, A., Pollack, J.L., Argüello, R.J., Meng, M.V., et al. (2022). Holistic characterization of tumor monocyte-to-macrophage differentiation integrates distinct immune phenotypes in kidney cancer. Cancer Immunol. Res. Canimm. *2021*, 0588. https://doi.org/10.1158/2326-6066.CIR-21-0588.

Mulder, K., Patel, A.A., Kong, W.T., Piot, C., Halitzki, E., Dunsmore, G., Khalilnezhad, S., Irac, S.E., Dubuisson, A., Chevrier, M., et al. (2021). Cross-tissue single-cell landscape of human monocytes and macrophages in health and disease. Immunity *54*, 1883–1900.e5. https://doi.org/10.1016/j.immuni.2021.07.007.

Müller, A., Brandenburg, S., Turkowski, K., Müller, S., and Vajkoczy, P. (2015). Resident microglia, and not peripheral macrophages, are the main source of brain tumor mononuclear cells. Int. J. Cancer *137*, 278–288. https://doi.org/10.1002/ijc.29379.

Nalio Ramos, R., Missolo-Koussou, Y., Gerber-Ferder, Y., Bromley, C.P., Bugatti, M., Núñez, N.G., Tosello Boari, J., Richer, W., Menger, L., Denizeau, J., et al. (2022). Tissue-resident FOLR2+ macrophages associate with CD8+ T cell infiltration in human breast cancer. Cell, S0092-8674220201-X. https://doi.org/10.1016/j.cell.2022.02.021.

Ovchinnikov, D.A., van Zuylen, W.J.M., DeBats, C.E.E., Alexander, K.A., Kellie, S., and Hume, D.A. (2008). Expression of Gal4-dependent transgenes in cells of the mononuclear phagocyte system labeled with enhanced cyan fluorescent protein using Csf1r-Gal4VP16/UAS-ECFP double-transgenic mice. J. Leukoc. Biol. *83*, 430–433. https://doi.org/10.1189/jlb.0807585.

Pal, B., Chen, Y., Vaillant, F., Capaldo, B.D., Joyce, R., Song, X., Bryant, V.L., Penington, J.S., Di Stefano, L., Tubau Ribera, N., et al. (2021). A single-cell RNA expression atlas of normal, preneoplastic and tumorigenic states in the human breast. EMBO J. *40*, e107333. https://doi.org/10.15252/embj.2020107333.

Picon-Ruiz, M., Morata-Tarifa, C., Valle-Goffin, J.J., Friedman, E.R., and Slingerland, J.M. (2017). Obesity and adverse breast cancer risk and outcome: mechanistic insights and strategies for intervention. CA *67*, 378–397. https://doi.org/10.3322/caac.21405.

Qian, B., and Pollard, J.W. (2010). Macrophage diversity enhances tumor progression and metastasis. Cell *141*, 39–51. https://doi.org/10.1016/j.cell.2010.03.014.

Qiu, X., Mao, Q., Tang, Y., Wang, L., Chawla, R., Pliner, H.A., and Trapnell, C. (2017). Reversed graph embedding resolves complex single-cell trajectories. Nat. Methods *14*, 979–982. https://doi.org/10.1038/nmeth.4402.

Roberts, A.W., Lee, B.L., Deguine, J., John, S., Shlomchik, M.J., and Barton, G.M. (2017). Tissue-resident macrophages are locally programmed for silent clearance of apoptotic cells. Immunity *47*, 913–927.e6. https://doi.org/10.1016/j.immuni.2017.10.006.

Roberts, E.W., Broz, M.L., Binnewies, M., Headley, M.B., Nelson, A.E., Wolf, D.M., Kaisho, T., Bogunovic, D., Bhardwaj, N., and Krummel, M.F. (2016). Critical role for CD103+/CD141+ dendritic cells bearing CCR7 for tumor antigen trafficking and priming of T cell immunity in melanoma. Cancer Cell *30*, 324–336. https://doi.org/10.1016/j.ccell.2016.06.003.

Sargeant, T.J., Lloyd-Lewis, B., Resemann, H.K., Ramos-Montoya, A., Skepper, J., and Watson, C.J. (2014). Stat3 controls cell death during mammary gland involution by regulating uptake of milk fat globules and lysosomal membrane permeabilization. Nat. Cell Biol. *16*, 1057–1068. https://doi.org/10.1038/ncb3043.

Schneider, C.A., Rasband, W.S., and Eliceiri, K.W. (2012). NIH Image to ImageJ: 25 years of image analysis. Nat. Methods *9*, 671–675. https://doi.org/10.1038/nmeth.2089.

Sharma, A., Seow, J.J.W., Dutertre, C.-A., Pai, R., Blériot, C., Mishra, A., Wong, R.M.M., Singh, G.S.N., Sudhagar, S., Khalilnezhad, S., et al. (2020). Onco-fetal reprogramming of endothelial cells drives immunosuppressive macrophages in hepatocellular carcinoma. Cell *183*, 377–394.e21. https://doi.org/10.1016/j.cell.2020.08.040.

Silva, H.M., Báfica, A., Rodrigues-Luiz, G.F., Chi, J., Santos, P. d'Emery A., Reis, B.S., Konijnenburg, D.P.H. van, Crane, A., Arifa, R.D.N., Martin, P., et al. (2019). Vasculature-associated fat macrophages readily adapt to inflammatory and metabolic challenges. J. Exp. Med. Jem.20181049 https://doi.org/10.1084/jem.20181049.

Stuart, T., Butler, A., Hoffman, P., Hafemeister, C., Papalexi, E., Mauck, W.M., Hao, Y., Stoeckius, M., Smibert, P., and Satija, R. (2019). Comprehensive integration of single-cell data. Cell *177*, 1888–1902.e21. https://doi.org/10.1016/j.cell.2019.05.031.

Summers, K.M., Bush, S.J., and Hume, D.A. (2020). Network analysis of transcriptomic diversity amongst resident tissue macrophages and dendritic cells in the mouse mononuclear phagocyte system. Plos Biol. *18*, e3000859. https://doi.org/10.1371/journal.pbio.3000859.

Trapnell, C., Cacchiarelli, D., Grimsby, J., Pokharel, P., Li, S., Morse, M., Lennon, N.J., Livak, K.J., Mikkelsen, T.S., and Rinn, J.L. (2014). The dynamics and regulators of cell fate decisions are revealed by pseudotemporal ordering of single cells. Nat. Biotechnol. *32*, 381–386. https://doi.org/10.1038/nbt.2859.

Van Nguyen, A., and Pollard, J.W. (2002). Colony stimulating factor-1 is required to recruit macrophages into the mammary gland to facilitate mammary ductal outgrowth. Dev. Biol. *247*, 11–25. https://doi.org/10.1006/dbio.2002.0669.

Wang, Y., Chaffee, T.S., LaRue, R.S., Huggins, D.N., Witschen, P.M., Ibrahim, A.M., Nelson, A.C., Machado, H.L., and Schwertfeger, K.L. (2020). Tissue-resident macrophages promote extracellular matrix homeostasis in the mammary gland stroma of nulliparous mice. ELife *9*. https://doi.org/10.7554/eLife.57438.

Wentworth, J.M., Naselli, G., Brown, W.A., Doyle, L., Phipson, B., Smyth, G.K., Wabitsch, M., O'Brien, P.E., and Harrison, L.C. (2010). Pro-inflammatory CD11c+CD206+ adipose tissue macrophages are associated with insulin resistance in human obesity. Diabetes *59*, 1648–1656. https://doi.org/10.2337/db09-0287.

Wu, S.Z., Al-Eryani, G., Roden, D.L., Junankar, S., Harvey, K., Andersson, A., Thennavan, A., Wang, C., Torpy, J.R., Bartonicek, N., et al. (2021). A single-cell and spatially resolved atlas of human breast cancers. Nat. Genet. *53*, 1334–1347. https://doi.org/10.1038/s41588-021-00911-1.

Xue, J., Schmidt, S.V., Sander, J., Draffehn, A., Krebs, W., Quester, I., De Nardo, D., Gohel, T.D., Emde, M., Schmidleithner, L., et al. (2014). Transcriptome-based network analysis reveals a spectrum model of human macrophage activation. Immunity *40*, 274–288. https://doi.org/10.1016/j.immuni.2014.01.006.

You, R., Artichoker, J., Fries, A., Edwards, A.W., Combes, A.J., Reeder, G.C., Samad, B., and Krummel, M.F. (2021). Active surveillance characterizes human intratumoral T cell exhaustion. J. Clin. Invest. *131*, e144353. https://doi.org/10.1172/JCI144353.

Zhu, Y., Herndon, J.M., Sojka, D.K., Kim, K.-W., Knolhoff, B.L., Zuo, C., Cullinan, D.R., Luo, J., Bearden, A.R., Lavine, K.J., et al. (2017). Tissue-resident macrophages in pancreatic ductal adenocarcinoma originate from embryonic hematopoiesis and promote tumor progression. Immunity *47*, 323–338. https://doi.org/10.1016/j.immuni.2017.07.014.

STAR★METHODS

KEY RESOURCES TABLE

REAGENT or RESOURCE	SOURCE	IDENTIFIER
Antibodies		
Anti-mouse CD45 (30-F11)	BD Biosciences	Cat#550994; RRID:AB_394003
Anti-mouse CD11b (M1/70)	BD Biosciences	Cat#563553; RRID:AB_2738276
Anti-mouse CD11b (M1/70)	BD Biosciences	Cat#564985; RRID:AB_2739033
Anti-mouse CD192 (SA203G11)	Biolegend	Cat#150605; RRID:AB_2571913
Anti-mouse CD206 (C068C2)	Biolegend	Cat#141723; RRID:AB_2562445
Anti-mouse CD64 (X54-5/7.1)	Biolegend	Cat#139314; RRID:AB_2563904
Anti-mouse Ly6C (AL21)	BD Biosciences	Cat#560596; RRID:AB_1727555
Anti-mouse Ly6G (1A8)	BD Biosciences	Cat#741813; RRID:AB_2871151
Anti-mouse I-A/I-E (M5/114.15.2)	BD Biosciences	Cat#563413; RRID:AB_2738190
Anti-mouse F4/80 (T45-2342)	BD Biosciences	Cat#565787; RRID:AB_2869711
Anti-mouse SiglecF (E50-2440)	BD Biosciences	Cat#740956; RRID:AB_2740581
Anti-rat AF647	Life technologies	Cat#A21247; RRID:AB_141778
Anti-IFNg Pe-Cy7 (XMG1.2)	BD Biosciences	Cat#557649; RRID:AB_396777
Chemicals, peptides, and recombinant proteins		
Dnase I	Roche	Cat#10104159001
Dispase II	Gibco	Cat#17105041
Collagenase IV	Gibco	Cat#17104019
Tissue freezing medium	Microm-Microtech	Cat#F/TFM-C
Formaldehyde	Sigma	Cat#47608
Polybeads carboxylate microsphere	Polysciences	Cat#07759-15
Sucrose	Biosolve	Cat#192223
Bovine serum albumin	Sigma	Cat#A3294
Vectashield with DAPI	VectorLabs	Cat#H-1200
Fetal bovine serum	Pan biotech	Cat#P30-3306
Trypsin-EDTA	Gibco	Cat#25200056
RPMI 1640 with glutamax	Gibco	Cat#61870010
CFSE	Thermofisher scientific	Cat#C1157
Brefeldin A	Thermofisher scientific	Cat#00-4506-51
Deposited data		
scRNAseq data	This paper	GEO: GSE184096
Experimental models: Cell lines		
PyMT cell line	(You et al.,2021)	Developed by MF. Krummel
Experimental models: Organisms/strains		
Mouse : Cx3cr1$^{EGFP/Kin}$	The Jackson laboratory	JAX : 005582
Mouse: Csf1rmApple	(Hawley et al., 2018)	Developed by D. Hume
Mouse: ΔCsf1rECFP	(Ovchinnikov et al., 2008)	Developed by D. Hume
Mouse: MMTV-PyMT-mCherry-OVA	(Engelhardt et al., 2012)	Developed by MF. Krummel
Software and algorithms		
ImageJ	(Schneider et al., 2012)	https://imagej.nih.gov/ij; RRID:SCR_003070
FlowJo v10	FlowJo, Treestar Inc.	https://www.flowjo.com; RRID:SCR_008520

(*Continued on next page*)

Continued

REAGENT or RESOURCE	SOURCE	IDENTIFIER
Prism v7	GraphPad Software	https://www.graphpad.com/scientific-software/prism/; RRID:SCR_002798
Imaris v8.0.2	Bitplane	http://www.bitplane.com/; RRID:SCR_007370
Zeiss Zen	Carl Zeiss	http://www.zeiss.com
Diva	BD Biosciences	http://www.bdbiosciences.com/us/instruments/clinical/software/flow-cytometry-acquisition/bd-facsdiva-software/m/333333/overview
OMIQ	OMIQ inc.	https://www.omiq.ai/
Rstudio		https://rstudio.com

RESOURCE AVAILABILITY

Lead contact

Further information and requests for resources and reagents should be directed to Alexandre Boissonnas (alexandre.boissonnas@upmc.fr).

Materials availability

This study did not generate new unique reagents.

Data and code availability

- Single-cell RNAseq data have been deposited at Gene Expression Omnibus and are publicly available as of the date of publication at the following accession number: GSE184096. GEO accession number is also listed in the key resources table.
- This paper does not report original code.
- Any additional information required to reanalyze the data reported in this paper is available from the lead contact upon request.

EXPERIMENTAL MODELS AND SUBJECTS DETAILS

Mice

Female MMTV-PyMT-P2A-mCherry-P2A-OVA (PyMT-ChOVA) (Engelhardt et al., 2012) for the scRNAseq were bred under specific pathogen-free conditions at the University of California, San Francisco Animal Barrier Facility. For flow cytometry and imaging analyses, Cx3cr1$^{EGFP/+}$ (Jung et al., 2000), Csf1r-Gal4VP16/UAS-ECFP (MacBlue (Ovchinnikov et al., 2008)), Csf1r-mApple (MacApple (Hawley et al., 2018)) and PyMT-ChOVA mice were intercrossed to generate MacBlue x Cx3cr1$^{EGFP/+}$ x PyMT-ChOVA and MacBlue x Cx3cr1$^{EGFP/+}$ x MacApple x PyMT-ChOVA mouse strains. These strains were bred at the Centre d'Exploration Fonctionnelle Pitié--Salpêtrière animal facility. To monitor TAM accumulation over time, between 14 and 40-week old mice were used. All mice were maintained under SPF conditions at 22°C and used after breast tumor development. OTI-1 RAG-2$^{-/-}$ mice were kindly provided by Sebastian Amigorena (Institut Curie, France). All experiment protocols were approved by the French animal experimentation and ethics committee and validated by Service Protection et Santé Animales, Environnement with the number #16890. Sample sizes were chosen to assure reproducibility of the experiments and according to the 3 Rs of animal ethic regulation. For scRNAseq, all mice were handled in accordance with NIH and American Association of Laboratory Animal Care standards, and experiments were approved by the Institutional Animal Care and Use Committee of the University of California, San Francisco.

PyMT tumor cell line

The PyMT cell line was derived from primary PyMT-ChOVA female breast tumor as described (You et al., 2021). Cells were cultured in RPMI-1640 with 10% fetal bovine serum, Na-Pyruvate, antibiotic, and anti-mycotic (GIBCO) and incubated at 37°C in 5% CO2. For orthotopic breast cancer model, 2.5 × 10^5 cells were injected in the mammary fat pad of 20-weeks old female.

METHOD DETAILS

Mouse tissue digestion and flow staining

Healthy mammary tissue, orthotopic and spontaneous tumors were processed the same way. Mammary tissues were harvested and enzymatically digested with 0.1 mg/mL DNase I (Sigma-Aldrich), 1.5 U/ml Dispase II (Gibco), and 200 U/ml Collagenase

Type IV (Gibco) in RPMI + glutamax (Gibco) for 30 min at 37°C under agitation. Samples were filtered using 70μm cell strainer and washed with FACS buffer (PBS, 0.5% FCS, 0.01% azide, 2mM EDTA). Cells were then washed and non-specific binding was blocked with Fcblock (BD biosciences). Cell surface proteins were then stained at 4°C for 30 min in Brilliant stain buffer (BD biosciences). Anti-CD45 (30-F11), anti-CD11b (M1/70), anti-Ly6C (AL21), anti-Ly6G (1A8), anti-SiglecF (E50-2440), anti-I-A/I-E (M5/114.15.2), anti-F4/80 (T45-2342) were purchased from BD Biosciences. Anti-CD64 (X54-5/7.1), anti-CD192 (SA203G11) and anti-CD206 (C068C2) were purchased from Biolegend. Cells were then washed once in FACS buffer and analyzed directly by flow cytometry. For cell cycle analysis, cells were fixed in 1% PFA for 10min at 4°C then washed in PBS, 2%FCS, 0.01% azide, 0.1% saponin. Cells were stained 1h at RT in 500μL PBS containing 2 μM topro-3 iodide (Molecular probes) and 10 μM RNase A (Boehringer). Calculation of absolute cell number was performed by adding to each vial a fixed number (10.000) of non-fluorescent 10μm polybead carboxylate microspheres (Polysciences, Niles, IL, USA) according to the formula: Nb of cells = (Nb of acquired cells x 10.000)/(Nb of acquired beads). Number of cells obtained for each sample was normalized per mg of tissue. Flow cytometry acquisition was performed on the flow cytometer FACS LSRFortessa X-20 (BD Biosciences, Franklin Lakes, NJ, USA) with DIVA (BD Biosciences) Flow Cytometry software. Flow cytometry data were analyzed with FlowJo software (Tree Star Inc., Ashland, OR, USA) or OMIQ (Omiq inc.) data analysis software for opt-SNE representations (https://omiq.ai, Santa clara CA).

Single cell RNA sequencing

Myeloid cells were sorted using a BD FACSAria Fusion (BD Biosciences, Franklin Lakes, NJ, USA), according to alive $CD45^+CD90.2^-B220^-NK1.1^-Ly6G^-CD11b^+$ or $CD11c^+$ from a mix of different tumors isolated from a pool of 4 PyMT-ChOVA mice. Among these, $CD11b^+$ and $CD11b^-$ myeloid compartment were individually sorted and processed for independent sequencing along with the bulk compartment. For the orthotopic model, only cells from the bulk gating were sorted from a pool of 5 different mice 15 days after tumor inoculation. After sorting, all cell preparations were pelleted and resuspended at 1 × 10^3cells/ml in 0.04%BSA/PBS and loaded onto the Chromium Controller (10X Genomics). Samples were processed for single-cell encapsulation and cDNA library generation using the Chromium Single Cell 3′v2 Reagent Kits (10X Genomics) according to manufacturer's protocol. The library was subsequently sequenced on an Illumina HiSeq4000 (Illumina).

Single cell data processing

Sequencing data was processed using 10X Genomics Cell Ranger V1.2 pipeline. The Cell Ranger subroutine mkfastq converted raw, Illumina bcl files to fastqs. Reads were then aligned with *count*, using the STAR aligner (Dobin et al., 2013) against the mm10 mouse genome. After filtering reads with redundant unique molecular identifiers (UMI), *count* generated a final gene-cellular barcode matrix. Both mkfastq and count were run with default parameters.

Cellular identification and clustering

For each sample, the gene/barcode matrix was passed to the R software package Seurat (v3.1.5) (Stuart et al., 2019) for all downstream analyses. We then filtered on cells that expressed a minimum of 200 genes and required that all genes be expressed in at least 3 cells. We also removed cells that contained >9% reads associated with cell cycle genes (Kowalczyk et al., 2015; Macosko et al., 2015). Count data was then log2 transformed and scaled using each cell's proportion of cell cycle genes as a nuisance factor (implemented in Seurat ScaleData function) to correct for any remaining cell cycle effect in downstream clustering and differential expression analyses. For the spontaneous PyMT model, Bulk, $CD11b^+$ and $CD11b^-$ enriched myeloid compartment datasets were merged for downstream analysis. Principal component (PC) analysis was performed on a set of highly variable genes defined by Seurat FindVariableGenes function. Genes associated with the resulting PCs were then used for graph-based cluster identification and subsequent dimensionality reduction using UMAP. Cluster-based marker identification and differential gene expression (DGE) were performed using Seurat FindAllMarkers for all between-cluster comparisons. Few clusters enriched for Epcam-Krt identified as tumor cells and enriched in ribosomal transcripts considered as dying cells were discarded from the analysis. Sub-clustering was performed by selecting cells from clusters of interest and the whole same processing was applied.

Gene signature overlay

Stromal macrophage, ductal macrophage, weaning, lactation, DC1 and DC2 were downloaded from (Dawson et al., 2020) (Table S1). We created a dataframe of gene values per cell from the input Seurat object. The calculate score was visualized on the UMAP with a saturation score between 0.5 and 0.7 for each signature. Density plot of genes and signatures were generated using the Nebulosa package (Alquicira-Hernandez and Powell, 2021).

Pseudotime analysis

Trajectory analysis was performed using the Monocle3 package (v1.0.0) (Cao et al., 2019; Qiu et al., 2017; Trapnell et al., 2014). Resolution was determined according to the clustering obtained with the Seurat package. Root node was assigned to monocytes for each analysis.

GSEA hallmark pathway analysis

The signature of each cluster was computed into GSEA (https://www.gsea-msigdb.org) for top100 hallmark pathways with FDR q-value < 0.05. From the generated list, only the hallmark with a k/K value >0.04 were selected. A score of 0 was set when the pathway was not found in the cluster. Heatmap was generated using the pheatmap package. k/K values of each pathway were used for the heatmap. Hierarchical clustering of centered and scaled gene expression was performed using complete linkage and Euclidean distance.

M1/M2 gene correlation

The list of commonly M1 or M2-associated genes was obtained from (Biswas and Mantovani, 2010; Cassetta et al., 2019; Cheng et al., 2021; Roberts et al., 2016) (Table S2). From this complete gene list (69 genes), 61 were recovered from the dataset and 50 out of the 61 were conserved using the Seurat FindVariableGenes function. Genes with lowest sct.mean (<0.02) for the dataset were discarded. We used the R package Stats (version 4.0.3) to calculate the correlation scores for each gene in individual cells. The *cor* function was used to compute gene correlation score with "spearman" as method. Resulting heatmap was generated with pheatmap. The same list was used to identify specific pattern in each cluster. The heatmap was generated using Doheatmap.

Homing molecule heatmap

Homing molecules were extracted from the HUGO database based on the manual selected lists of Regulators of G protein signaling, integrins, selectins, and chemokine receptor families (Table S3). The most differentially expressed genes among clusters from this list were determined using FindAllMarkers from Seurat and the heatmap was generated using Doheatmap.

Transcription factor analysis

We applied murine version of DoRothEA (version 1.2.1) package in combination with VIPER package (version 1.24.0) on single sample matrices (genes in rows and single cells in columns) containing normalized gene expression scores scaled gene-wise. Transcription factors with lowest confidence levels listed in the corresponding gene expression matrix were discarded from the analysis. VIPER provides a normalized enrichment score (NES) for each TF which we consider as a metric for the activity. Resulting heatmap was generated with pheatmap.

Human data processing

scRNAseq dataset were obtained from (Pal et al., 2021) (GSE161529). All 32 files corresponding to female tumor samples of all types were pre-processed with the same pipeline than mouse scRNAseq. After cleaning the data, myeloid cells identified by the expression of *PTPRC*, *CD68*, *CSF1R*, *FCGR1A* of each individual tumor were subsampled. Tumors containing less than 300 myeloid cells were excluded for downstream analyses. Samples were combined using anchor-based integration method from Seurat. The integrated data were used for downstream analysis, for which the same pipeline than mouse analysis was applied.

Co-culture experiment

Each TAM subset was sorted using a BD FACS Aria III according to alive $CD45^{+}Ly6G^{-}Ly6C^{-}CD64^{+}$, CD11b level and fluorescent reporter expression from pooled tumors of PyMTFluo-ChOVA mice. OT-I T cells were isolated from axillary and brachial lymph nodes and incubated in 1mM CFSE for 5min at 37°C and washed in PBS/FCS. Cells were plated at a 5:1 T cell/TAM ratio in 96 round well plate in RPMI with 10% FCS with antibiotics/antimycotics. 1μM ovalbumin peptide SIINFEKL was added to each well. Plates were incubated for 72 h at 37°C–5%C CO_2. For the last three hours of culture, 5μg/ml of brefeldin A was added to each well for IFNγ staining.

Multi-photon imaging

The two-photon laser-scanning microscopy (TPL SM) set-up used was a 7MP (Carl Zeiss) coupled to a Ti: Sapphire Crystal multi-photon laser (ChameleonU, Coherent), which provides 140-fs pulses of near-infrared light, selectively tunable between 680 and 1050 nm and an optical parametric oscillator (OPO-MPX, Coherent) selectively tunable between 1,050 and 1,600 nm. The NLO and the OPO beams were spatially aligned and temporally synchronized using a delay line (Coherent) allowing CARS imaging approach (Boissonnas et al., 2020). The excitation wavelength was 840 nm for the NLO beam and 1104 nm for the OPO beam to detect the vibrational signature of lipid rich structures at a frequency of 2846 cm^{-1} with an emission wavelength at 678 nm. The system included a set of external nondescanned detectors in reflection with a combination of an LP-600-nm followed by LP-462-nm and LP-500-nm dichroic mirrors to split the light and collect the second harmonic generation signal (SHG) with a 417-/60-nm emission filter, ECFP with a 480-/40-nm emission filter, EGFP with a 525-/50-nm emission filter, mCherry or Apple with a 624-/40-nm emission filter and CARS or blue evans signal with an LP 645nm emission filter. For live imaging, mice were anesthetized and maintained during the imaging period with 2% isoflurane in medical air. An incision of the skin was performed at the level of the breast tumor and an imaging window was positioned to stabilize the tissue from breathing and drifting artifacts. Local temperature was monitored and maintained at 32°C using an incubation chamber. To define the tumor vasculature, Evans Blue was injected i.v. before the imaging session. Real time movies were performed by imaging every 30s by 5 consecutive 3μm z spacing image stack (total 12μm thickness). Static 3D images were performed on 100μm thick cryosections by 1μm z spacing image stack (up to 20μm thickness). For all images

the objective was a water immersion, plan apochromat ×20 (numerical aperture = 1). 3D reconstructions and mask rendering were done using Imaris software (Bitplane).

Epifluorescent imaging of tumor sections

In brief, mammary tissue and tumors were harvested and fixed in 2% PFA for 6 h and then incubated in 30% sucrose-PBS overnight at 4°C before being embedded in OCT-freezing medium (Microm microtech) and frozen at −80°C. Sectioning was completed on an HM550 Cryostat (Thermo Fisher) at −20°C; 5-μm or 100-μm sections were collected on Superfrost Plus Slides (Thermo Fisher Scientific) and stored at −20°C until use. Tissue sections were rehydrated with 0.5% Triton-PBS during 10 min. For CD11b staining, a first block step was performed with 3% BSA solution during 2h, followed by 2h incubation at room temperature with the primary antibodies (Rat anti-mouse CD11b, clone M1/70; BD Biosciences). Secondary antibody incubation was performed using anti-rat AF647-conjugated antibody 1h30 at room temperature (Jackson ImmunoResearch Laboratories). Slides were counterstained and mounted with Vectashield Mounting Medium with DAPI (Vector Laboratories). Epifluoresent images were acquired on a Zeiss Axio Z1 fluorescent microscope (Carl Zeiss, Germany) using Zen software. ECFP, EGFP, DAPI, mCherry, and AF647 signals were acquired using a combination of LED Colibri 7 and emission filters: LED 385 nm, EmBP 450/40 for DAPI; LED 430nm, EmBP 480/40 for ECFP; LED 475 nm, EmBP 525/50 for EGFP; LED 511nm, EmBP 605/70 for Apple; LED 555nm, EmBP 647/57 for mCherry; LED 630nm, EmBP 690/50 for AF674. Image quantifications were performed using histo-cytometry based approach. Briefly, after masking the cells as individual objects based on DAPI, EGFP or mCherry signal for tumor nodule contouring using Imaris software, fluorescent signals from all channels and spatial coordinates were extracted and transformed into fcs file for cytometry-based analysis using FlowJo. Distance of $EGFP^+$ and $ECFP^+$ TAMs to the tumor was calculated using the distance transformation module from Imaris software. CD11b quantification was performed by surfacing TAMs based on the EGFP channel. CD11b expression on $EGFP^+$ TAMs was measured using the sum intensity of the CD11b channel parameter gated on different regions of the tumor (hyperplastic, adenoma, malignant, according to their histological characteristics (Lin et al., 2003)). Acquisition and analysis settings were identical for both isotype and CD11b staining. Between three and six fields were chosen for each lesion type per mouse (n = 6 mice). All histological quantifications are presented as a mean of the different fields for each mouse.

QUANTIFICATION AND STATISTICAL ANALYSIS

All statistical analyses were performed with Graphpad Prism 7 for flow cytometry and imaging, and R for scRNAseq analysis. Multigroup analysis of variances were performed, and one-way or two-way ANOVA tests were performed followed by Turkey post test for Gaussian distribution or Kruskall-Wallis followed by Dunn's multiple comparisons. For simple comparison analysis, Mann-Whitney was performed to compare nonparametric distribution. For correlation analysis, Pearson correlation was calculated *, $p < 0.05$; **, $p < 0.01$; ***, $p < 0.001$. Sample sizes are indicated in each figure legend.